

Joint Bulk and Shear Wave Analysis of Mantle Properties with the new GLAD-M35 Full-Waveform Tomography Model

Ramon Margarit

Dr. Laura Cobden

Under Review

Guided Research



Earth Science
Utrecht University
The Netherlands
July 13, 2024

Abstract

This research project aims to explore Earth's lower mantle properties using a quantitatively joint analysis of bulk and shear absolute wave velocities using the new GLAD-M35 full-waveform tomography model. By constraining simultaneously bulk and shear wave speeds and using absolute speeds rather than perturbations, we showed that in order to fit the tomographic velocities hypothetical mantle models containing an Iron Spin crossover (ISC) in ferropericlase are needed. Furthermore, we compare these new results obtained from the new tomography model to the preceding one, GLAD-M25, and we evaluate different thermochemical properties derived from the selected thermochemical mantle models. It's also shown how the lowermost mantle needs an extra enrichment in silica to fit the wave speeds; these silica enriched regions may be remains that would have survived from an ancient magma ocean.

Under Review



Plain Language Summary

This study examines the Earth's interior using a more detailed new mantle model. It is shown that in order to have an almost perfect agreement with the waves speeds travelling through Earth's interior, a quantum effect that occurs at very high pressure on the iron of one of the main components of the Earth's interior must be considered. Including these phenomena, a more detailed mantle model can be obtained, providing more accurate insight into the current properties of the Earth mantle. This will allow future studies to better understand the evolution and interior of our planet.

Under Review

Contents

1	Introduction	6
2	Methodology	8
2.1	Prior Models	8
2.2	Selection Algorithm	9
3	Iron Spin Transition	12
4	Results	15
4.1	Restricted Prior	15
4.2	Broad Prior	28
4.3	Results Summary	32
5	Discussion	33
6	Conclusion	35
A	Appendix	36
	Bibliography	40

List of Figures

2.1 Bulk and Shear wave speeds on scatter plots for seismic tomography GLAD-M25 and GLAD-M35 -(Black Clouds) versus the thermochemical prior models with and without ISC -(Color Clouds).	9
2.2 Workflow of the selection algorithm. Target and Prior shear and bulk velocities are confronted to obtain a joint distribution. The Prior values are confronted to this distribution to select the final models.	11
3.1 Figure taken from Lin et al. (2013) Mineralogical model as a function of pressure and depth based on pyrolite composition models.	12
3.2 Figure adopted from (Lin et al., 2013) showing the spin crossover of iron in Fe^{2+} in octahedra cell ferropericlase along the mantle geotherm. It contains data from (Lin et al., 2007), (Iakov et al., 2011), (Sturhahn et al., 2005), (Wu et al., 2009) and (Tsuchiya et al., 2006).	13
4.1 Accepted values for GLAD-M25 and GLAD-M35	15
4.2 Bulk and Shear wave speeds fit with and without Iron Spin Crossover in Restricted Prior for GLAD-M35 and GLAD-M25.	17
4.3 Adiabatic Temperature Profile in the Earth mantle constructed with data from (Katsura, 2022, Table 3)	18
4.4 Temperature Distribution as function of depth with and without ISC for GLAD-M25 and GLAD-M35.	19
4.5 Silica distribution as function of depth for Prior with and without ISC for GLAD-M25 and GLAD-M35.	20
4.6 Ferropericlase distribution as a function of depth for Prior with and without ISC for GLAD-M25 and GLAD-M35.	22
4.7 Bridgemanite distribution as function of depth for Prior with and without ISC for GLAD-M25 and GLAD-M35.	23
4.8 Post-perovskite distribution as function of depth for different prior with and without ISC for GLAD-M25 and GLAD-M35.	24
4.9 MgO distribution as function of depth for Prior with and without ISC for GLAD-M25 and GLAD-M35	26
4.10 Iron Oxide distribution as a function of depth for Prior with and without ISC for GLAD-M25 and GLAD-M35.	27
4.11 Accepted values for GLAD-M25 and GLAD-M35 for Broad Prior.	28
4.12 Bulk and Shear wave speeds fit with and without Iron Spin Crossover in Broad Prior for GLAD-M35 and GLAD-M25.	29

4.13 Silica distribution as function of depth for Prior with and without ISC for GLAD-M25 and GLAD-M35.	30
4.14 Temperature Distribution as a function of depth with and without ISC for GLAD-M25 and GLAD-M35.	31
A.1 Histograms showing the iterative fitting process on histograms for shear wave values at 1500km depth in GLAD-M35.	37
A.2 Histograms showing the iterative fitting process on histograms for bulk wave values at 1500km depth in GLAD-M35.	38
A.3 Final Accepted histograms for the joint inverted Shear and Bulk waves at 1500km depth without ISC present on the Prior model for GLAD-M35.	39

Under Review

Chapter 1

Introduction

Understanding the thermochemical composition and evolution of the Earth's mantle is key to shape the evolution of our planet. The lower mantle represents more than half of the Earth's interior volume and plays a significant role in key processes such as the exchange of mass and heat between the surface and the outer core. Although occasionally some inclusions from the lower mantle reach the surface, for instance, inside diamonds, these are unlikely to represent the mantle's overall composition. Therefore, there is a need to use indirect techniques to study the interior of our planet.

the study of ?

Seismology offers a valuable method for exploring mantle dynamics, composition, and evolution. However, to provide an accurate interpretation of the wave speed variations, a big effort must be made to understand the underlying physical and chemical compositions and to separate different contributions to wave speeds.

Global tomographic models of the Earth generate detailed maps of the lower mantle, presenting independent assessments of compressional and shear wave velocities. Yet, extracting a conclusion from these tomographic models is a challenging task. The complexity arises because seismic velocities are significantly affected by temperature, composition, and pressure. Different thermochemical factors can have contrasting impacts, creating trade-offs that culminate in a distinct wave-speed value (Deschamps & Trampert, 2003). In other words, interpreting seismic wave speeds alone is a non-unique problem, where the wave speeds present lateral variations that can be produced by a trade-off of thermochemical processes, and thus, discerning between the different processes is a challenging task.

Full waveform inversion (FWI), opposed to traditional body wave seismology that uses a reduced selection of travel-time measurements, utilizes all the information available in a seismogram to discern the structure and dynamics of the Earth. Furthermore, traditional seismology usually works with 1D reference models. Nonetheless, seismic data behaves non-linearly on the wave speed structure. This issue can be treated when using a full waveform inversion, which has been proven to produce models with much higher amplitude variations than traditional methods (Trampert & Fichtner, 2013). FWI covers the complexity of 3D seismic-wave propagation and produces enhanced seismic images and with higher resolution to study Earth's interior across all scales (Tromp, 2019).

Three-dimensional models are particularly useful to identify temperature-dependent phenomena that are not evident in 1D spherical averages. Moreover, FWI has proved its efficacy in revealing chemical and mineralogical phase transitions as well as spin transformations within the mantle, as demonstrated by Cobden et al. (2024)

Building on this previous work, this current study aims to constrain bulk and shear absolute wave speeds over the same frequency range, demonstrating the feasibility of distinguishing variations in composition and the electronic spin crossover in ferropericlase using a more advanced full waveform tomography model, the GLAD-M35 (Cui et al., 2024) which consists of 35 iterations, 10 more iterations than the previous model and some uncertainty analyses. Our goal is to determine whether we can replicate the results from Cobden et al. (2024) using the preceding GLAD-M25 tomography model and investigate if the Iron Spin Crossover is also visible in the new tomography model, GLAD-M35. Furthermore, we aim to assess various mineralogical assemblages for the mantle after fitting the wave speeds obtained from our Prior models to the new tomography model.

Under Review

Chapter 2

Methodology

2.1 Prior Models

The mineralogical ~~assemblage~~ set of models (here called Priors) used to fit the target tomographic velocities are taken from (Cobden et al., 2024). These prior models were obtained using thermodynamic modeling corresponding to ~~different thermochemical structures~~. In this work, two different priors are used. The first Prior model used (here called Restricted Prior) includes some variations in chemistry, covering variability in xenoliths (Afonso et al., 2013) but MORB-like models are restricted (Deschamps et al., 2019). The second Prior (here called Broad Prior), on the other hand, consists of large variations in chemistry including ranges of mantle xenoliths and even models of chondritic Earth. Using both GLAD-M25 and GLAD-M35 tomography models, depths from 1000 to 2800 km are analyzed in steps of 100 km, this is, 19 depths in total. Priors consist of a maximum of 750.000 models in total for every depth (Cobden et al., 2024). One could suggest that more models would be needed to cover an even larger range, but more models would not make a difference since our Metropolis-Hastings algorithm converges with the given Priors.

The use of P-waves ($v_p = \sqrt{\frac{K+\frac{4}{3}G}{\rho}}$) can be challenging due to the influence of both the bulk and shear modulus, making it difficult to discern between different physical processes. Instead, in this work, bulk and shear waves are used. Isolating the bulk and shear modulus provides more information on the influence of thermochemical factors to wave speeds. Bulk and shear wave speeds are respectively:

$$v_\Phi = \sqrt{\frac{K}{\rho}} \quad \text{and} \quad v_s = \sqrt{\frac{G}{\rho}} \quad (2.1)$$

Where K, G, ρ are the bulk modulus, shear modulus and density respectively.

In the next figure 2.1, we plotted in scatter plots the Restricted Prior data velocities and the target tomography velocities. Color clouds correspond to the mineralogical Priors, and in black, the corresponding velocities taken from the GLAD-M25 and GLAD-M35 velocity models. A cloud of points is generated every 300 km depth. In the left columns, data without Iron Spin Crossover (ISC) are plotted and on the right column, plots with the Prior including the ISC are shown.

It can be seen that including the ISC, black clouds are completely fitting inside the mineralogical priors, meaning that preliminary, velocities from both tomography models can be fitted by the giving Priors.

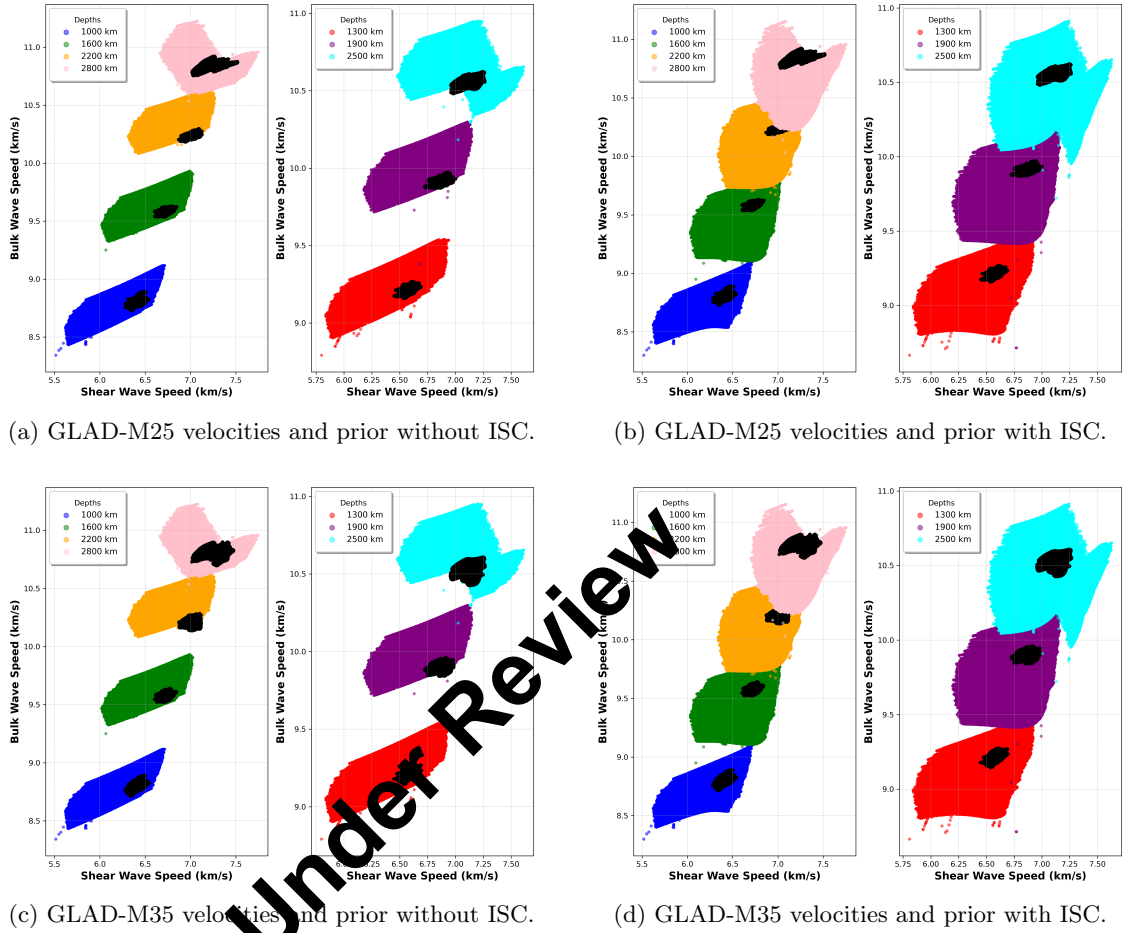


Figure 2.1: Bulk and Shear wave speeds on scatter plots for seismic tomography GLAD-M25 and GLAD-M35 -(Black Clouds) versus the thermochemical prior models with and without ISC -(Color Clouds).

Again, looking at the different depths in the previous figure, it can be seen how the black clouds of data velocities from the two tomography models cannot be fitted by the Restricted Prior without ISC at the bottom of the mantle. Nevertheless, when ISC is included in the Prior models, the color points are spread out covering the whole velocity ranges and making it possible to fit the target velocities. Qualitatively, there is not a big difference between the new and the former tomography models. Both models show how depth 2800 km cannot be completely fit by the prior data since the color cloud cannot fit completely the black cloud. This simple but straight forward results may indicate that more variability would be needed to fit the models in the lowermost mantle. This issue will be further addressed in this study.

2.2 Selection Algorithm

As mentioned in the previous section, the Prior models consist of a large number of models covering large variability of chemical models seen in the literature. Thus, the most appropriate models were selected and the worst-fitting models were discarded. One successful approach applied to geophysical inverse problems is the Monte Carlo method (Sambridge & Mosegaard, 2002). An old but powerful development in this area is the Metropolis algorithm, designed to sample a space according to a Gibbs-Boltzmann distribution asymptotically. This algorithm consists of a biased random walk, with each step (iteration) governed by simple probabilistic rules.

Following the approach stated almost 30 years ago by Mosegaard and Tarantola (1995) the algorithm first uses the a priori models described in the previous section, taken from Cobden et al. (2024). The second component of our algorithm evaluates and either accepts or rejects the proposed moves of the a priori random walk. This decision is based on the models' ability to reproduce the joint bulk and shear wave speeds in the tomographic models GLAD-M25 and GLAD-M35 from 1000 to 2800 km depth. In order to evaluate the output models from the Metropolis-Hastings algorithm, we can compare the histograms from the target distributions (GLAD-M25 and GLAD-M35) against those from the Prior distribution (the mineralogical models). An illustration of the iteration histograms can be seen in the Appendix A.2.

The joint inversion process starts by dividing the frequency distributions of the target tomographic velocities by the prior frequency distribution, separately for shear waves and bulk waves. Then, these adjusted frequency distributions for each wave type are multiplied together to form a combined inversion. Once the joint distribution is obtained, the acceptance criteria from the Metropolis-Hastings (MH) algorithm are applied. Prior distributions are confronted with the joint target distribution. The output is a collection of models that meet the acceptance criteria after several iterations. These selected models for either shear wave speeds or bulk wave speeds can be visualized and analyzed using compiled histograms instead of local wave speeds, as the impact of uncertainties in mineral physics or tomography is shown to diminish Cobden et al. (2024).

The algorithm selects the most appropriate prior models depending on the bar heights in the histograms. Each histogram's bin is evaluated in sequence. Firstly if the range of the prior is larger than our desired tomographic target values, the algorithm discards the models. Next, it evaluates the frequency of the individual bars. In the case when the prior's frequency is higher than the target for a given bar, the Metropolis-Hastings routine eliminates a portion of the prior thermochemical model based on a random choice. If target values have a larger frequency than the Prior values, then the models are selected. This process is repeated iteratively until an optimal fit to the target distribution is achieved or in the last case when the next step would start decreasing the fit. It has been shown that the Metropolis algorithm is optimal due to its intrinsic property of being as exploratory as possible, in other words, it requires for a transition to take place that the likelihood increases. The Metropolis-Hastings algorithm is a particular example of a Markov chain Monte Carlo (MCMC) method. Within the framework of random walks through model space, a Markov chain represents a sequence of models where the next model depends only on the current model and not on any prior ones. This implies that the progression of a Markov chain from a specific model is entirely determined by that model alone, with no memory of earlier models. This algorithm constructs a Markov chain because the proposed move is independent even of the current model, and the accepted move of a proposed step is only based on the likelihood ratio between the current and proposed models (Fichtner, 2021).

As demonstrated in previous studies such as (Cobden et al., 2012), these selected distributions provide valuable and useful information on the temperature and mineralogical properties that influence seismic velocities.

Next figure 2.2 illustrates the workflow of the process. Also, an example of the histograms created by this algorithm, can be visualized in the figures in the Appendix A.1, A.2 and A.3 showing the iterative steps to fit the tomographic model for a given depth and thermochemical prior distribution for the GLAD-M35 tomography model.

The treatment of data and the algorithm are implemented in Python language.

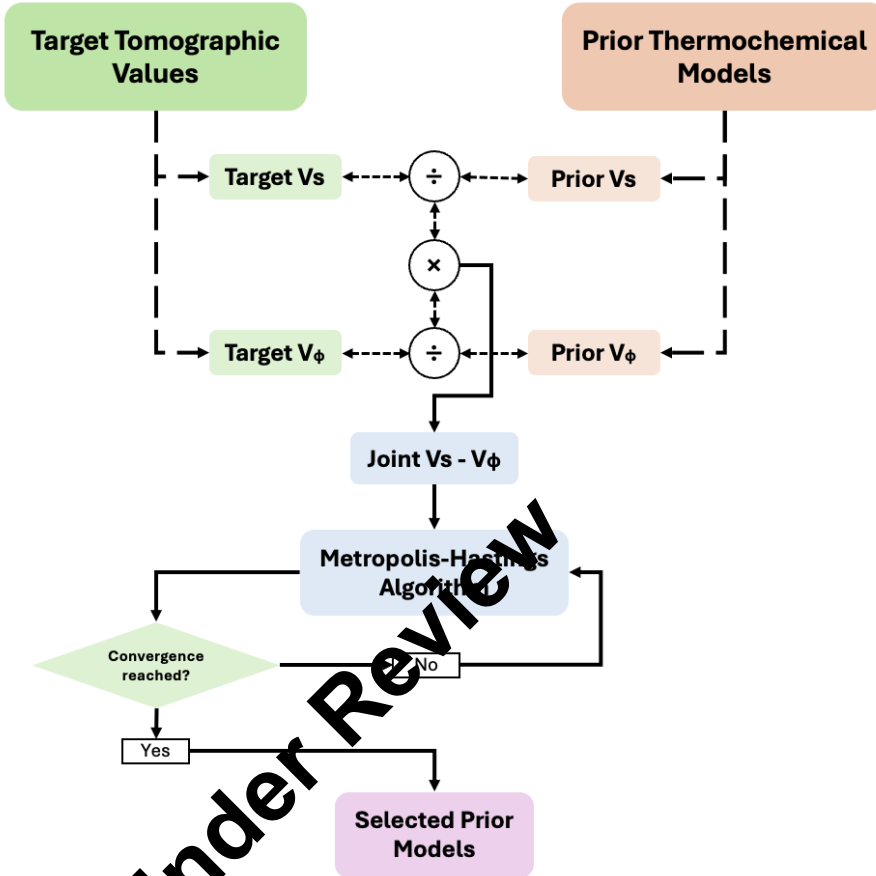


Figure 2.2: Workflow of the selection algorithm. Target and Prior shear and bulk velocities are confronted to obtain a joint distribution. The Prior values are confronted to this distribution to select the final models.

Chapter 3

Iron Spin Transition

To accurately interpret observations of the lower mantle it is important to determine the thermochemical properties of the most common mineral phases present under extreme pressure and temperature conditions in this region of the Earth. These mineral phases include magnesium silicate perovskite (Pv) ($(Mg, Fe)SiO_3$) (the magnesium end-member is called bridgmanite), occupying around 70% of the bulk volume, and ferropericlase (Fp) ($(Mg, Fe)O$) being around 20% in volume of the mantle.

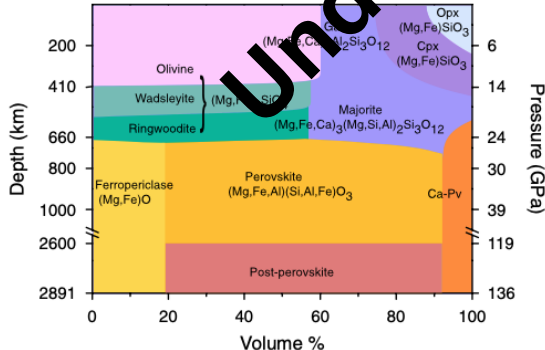


Figure 3.1: Figure taken from Lin et al. (2013). Mineralogical model as a function of pressure and depth based on pyrolite composition models.

Understanding the configuration of the valence orbital of the atoms is particularly important. Experimentally, it had been suggested that iron in ferropericlase could undergo a spin state change in P-T conditions through the mantle. Silicate perovskite changes into post-perovskite (pPv) polymorph under the P-T conditions of the lower mantle, corresponding to the D'' region (Murakami et al., 2004).

Iron is one of the most abundant transition metals found in the Earth's interior. It has 3d valence shell orbitals that can be partially filled with electrons. Iron shows two main valence states, Fe^{2+} with 6 electrons occupying the valence shell, and Fe^{3+} with only 5 electrons on the outermost orbital. Ferropericlase in the mantle presents mainly the Fe^{2+} state.

In ferropericlase, the Fe^{2+} ion in the octahedral unit cell structure can exist in a high-spin (HS) state, where four electrons occupy unpaired orbitals and two are paired. In the low-spin (LS) state, all six electrons are paired and occupy only three orbitals. According to the theoretical calculations by Badro et al. (2003), this pressure-induced spin transition from HS to LS for iron in ferropericlase can occur within the pressure domain of the lower mantle. This transition can happen when the thermal energy, at the temperature and pressure conditions of the mantle is enough to overcome the energy difference between the two quantum states. Also, experimental measurements have confirmed that the spin state of iron in ferropericlase can transition from HS to LS in the 60-70 GPa pressure, depths of approximately 2000 kilometers within the Earth's lower

mantle (Badro et al., 2003).

Fe^{3+} in bridgmanite most likely remains in HS state in a dodecahedra cell structure while the HS to LS transition in octahedral would occur at pressures of the mid-mantle (Lin et al., 2013). In contrast, iron in bridgmanite would remain in the HS state at pressures exceeding 1000 GPa (Badro et al., 2003). In post-perovskite, iron Fe^{3+} would remain in LS the whole lowermost mantle. Additionally, Badro et al. (2004) identified a second transition occurring at 120 GPa, corresponding to a depth of 2600 km. Future research could address the issue of finding the iron electronic crossover of these minerals in Earth mantle with the new tomographic model.

Along the mantle geotherm, the ISC is present over a large interval of depths, making it difficult to discern. The Spin Transition Zone (STZ), the zone where the spin transition occurs, becomes gradual and broad under the temperature conditions in the mantle. This is the reason why the crossover effect in 1D reference models difficult to discern. Interestingly enough, previous studies have suggested that a possible magnetic collapse of ferrous iron could theoretically explain the seismic variations observed in the core-mantle transition (Cohen et al., 1997).

Quantitatively, past works have defined the fraction of the low spin state n_{LS} as:

$$n_{LS} = \frac{1}{1 + \exp\left(\frac{\Delta G(P,T)^*}{T}\right)} \quad (3.1)$$

Where $\Delta G(P,T)^*$ is the Gbp. free energy between the two valence states (Wentzcovitch et al., 2009).

Next Figure 3.2, taken from (Lin et al., 2013) shows experimental results highlighting the fraction of the low spin state in ferropericlase.

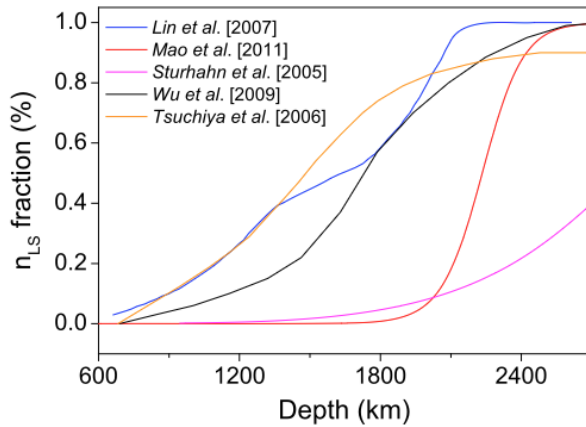


Figure 3.2: Figure adopted from (Lin et al., 2013) showing the spin crossover of iron in Fe^{2+} in octahedra cell ferropericlase along the mantle geotherm. It contains data from (Lin et al., 2007), (Mao et al., 2011), (Sturhahn et al., 2005), (Wu et al., 2009) and (Tsuchiya et al., 2006).

This previous figure shows the fraction of atoms in the Low State is significant under conditions of the lower mantle. As seen from these results, under the physical conditions of the lower mantle, the iron crossover takes place over a broad and smooth region through the whole lower mantle instead of a sharp discontinuity. Different theoretical experiments show different depths at which the ISC happens, showing some discrepancy among them.

Additionally, this electronic transition between states can also have a great impact on the atomic radii of iron ions. According to Lin et al. (2013), the 6d octahedral cell in Fe^{2+} is reduced

from 0.78Å to 0.61Å from high state to low spin state respectively. This is a difference of 22% in the radius or around a 50% reduction in volume between both states. Furthermore, having pair or unpaired valence electrons can lead to broad variations in physical properties such as density, bulk modulus electrical conductivity, and chemical properties of the minerals in the lower mantle.

Although this study did not aim to demonstrate the geographical diversity of sound waves, Marquardt et al. (2009) estimated that the ISC appears to influence the elastic shear anisotropy in ferropericlase. The LS state shows a maximum elastic shear anisotropy approximately three times that of bridgemanite and post-perovskite, making it a strong candidate to explain seismic observations of shear anisotropy in the lowermost mantle (Lin et al., 2013).

Shephard et al. (2021) adopted a different method to locate the ISC in the lower mantle. They identified regions of fast and slow velocities for P and S waves by utilizing individual tomography models. In this study, intervals of 50km across the mantle were used to identify patterns in both seismic waves such as a non-agreement between P and S wave velocities around 1400 and 2200 km depth (Shephard et al., 2021). However, they used four different models for P-wave and S-wave, being common for the two wave types only one of them (HMSL-P06 and HMSL-S06). Furthermore, to establish the influence of the ISC, they analyzed the geographic similarity between the individual P and S waves. In other words, they use a so-called "vote map" to study the surface area provided by these models, where having 4 votes (4 models in agreement), indicate the existence of fast anomalies. However, as it is stated in their paper, each tomography model uses different types of input data, parametrization and regularization, making this approach not convenient to further analyzes.

In contrast, this study ensures full consistency between v_p and v_s waves. Rather than using a "vote map," it quantitatively compares the fit of mantle models with and without an ISC.

Chapter 4

Results

The algorithm provides a wide range of selected models as output. In this section, we included distributions as a function of depth for different physical and thermochemical properties of the lower mantle. Results include prior with and without the Iron Spin Crossover that are used to fit both target models, GLAD-M25 and GLAD-M35. The first section contains the Restricted Prior and then the next section, the Broad Prior.

4.1 Restricted Prior

First, the next figure, Fig. 4.1, showcases an interesting result coming out of the selection algorithm, this is, the number of accepted values as a function of depth for both tomography models GLAD-M25 and GLAD-M35 with and without Iron Spin Crossover.

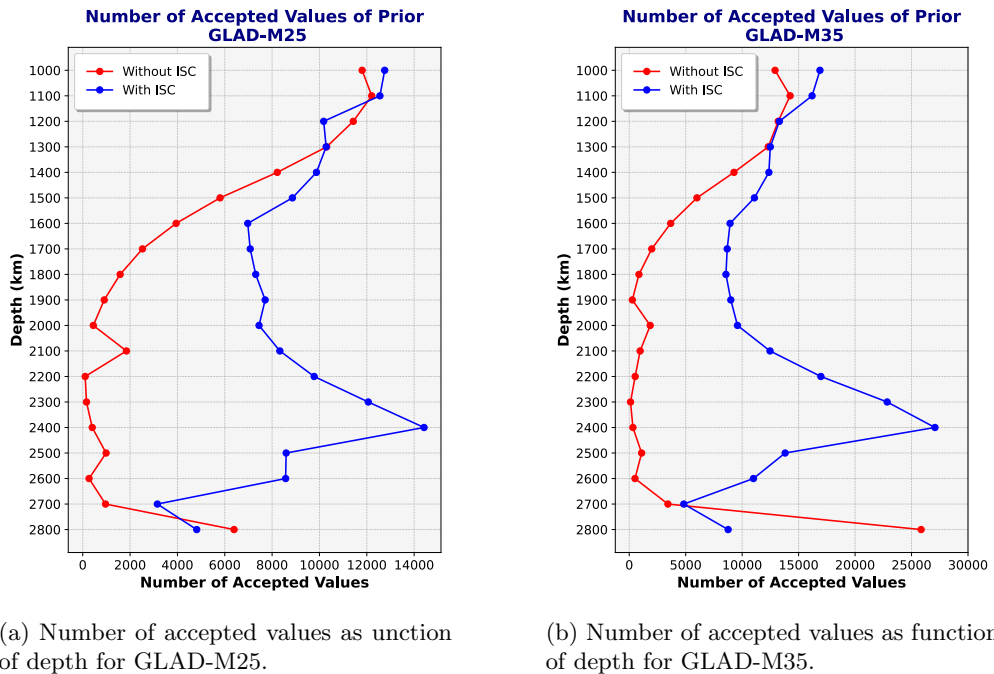


Figure 4.1: Accepted values for GLAD-M25 and GLAD-M35

It is consistent between both tomography models that the algorithm systematically accepts more values of the Prior with ISC. Without ISC, less than 2000 values are accepted in both tomography models between 1800 and 2700 km. However, it is significant the increase in accepted

values at 2400 km depth when ISC is included. As a whole, the algorithm systematically selects a larger amount of models for all depths when ISC is included.

This previous figure is consistent with the next figure 4.12 which quantitatively evaluates the fit of the Prior values to the joint velocity values as a function of depth. This percentage of fit corresponds to the last (the selected) iteration of the MH algorithm.

The red line represents the fit without ISC, and in blue, it is represented the fit including the quantum effect.

It can be seen how the fit is relatively good for the lower mantle until it reaches around 2000 km depth having a minimum fit at 2100 km for GLAD-M25. In the case of the new GLAD-M35, this behavior is shared with the old one, but our algorithm provides the worst fit at 2300 km depth.

Consistently with the previous mineralogical study cited in the previous section, without ISC, bulk and shear velocities cannot be fit in the area where theoretically ISC is supposed to be present in the mantle. Nevertheless, when the ISC is included in the Prior models, tomographic velocities can be almost perfectly fitted through the whole mantle.

This is consistent between both tomographic models. However, as a detail, the worst fit without ISC is moved from 2100 km depth for the old tomographic model to 2300 km depth for the new model. Below 2500 km, the fit v_p and v_s is significantly worse for both tomographic models, this may be due to the effect of the silica enrichment when near the Core-Mantle Boundary (CMB).

These results are significant since we are able to show that the observed tomographic values can be fitted with the preceding GLAD-M25, corroborating the results form Cobden et al. (2024) and confirming that this quantum effect is indeed visible in a more detailed tomographic model, the GLAD-M35 since including the ISC in the prior models results in a perfect fit.

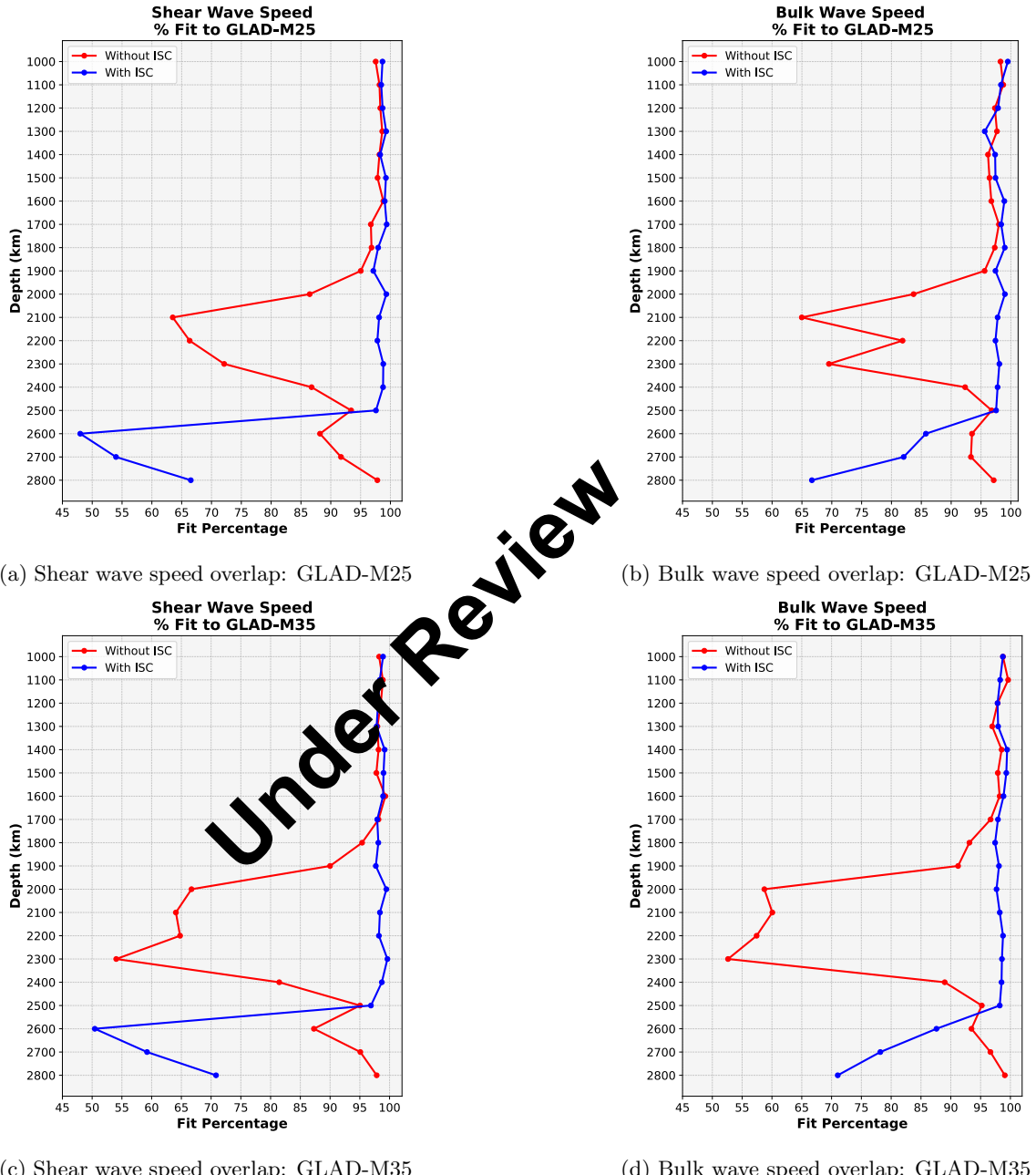


Figure 4.2: Bulk and Shear wave speeds fit with and without Iron Spin Crossover in Restricted Prior for GLAD-M35 and GLAD-M25.

Determining the precise temperature of the mantle is undoubtedly important for different geodynamical simulations. Next figure 4.3 shows the distribution of temperature as a function of depth produced with data from (Katsura, 2022, Table 3). When these results are compared with our results in next Fig. 4.4, it can be seen that the distributions without ISC show unrealistic temperatures. Only when incorporating the ISC, the obtained temperatures in our study show realistic values for both GLAD-M25 and GLAD-M35.

The temperature distribution in the next figure shows a good agreement through all depths until reaching the lowermost mantle. The disagreement between (Katsura, 2022) and our results is around 1000K for this region.

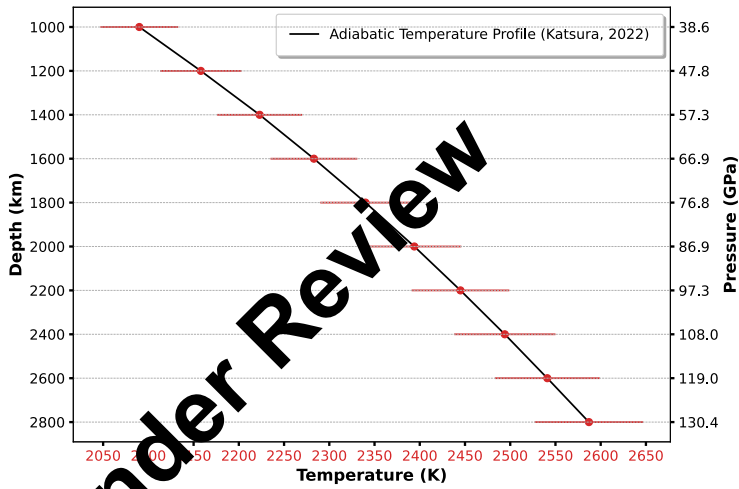
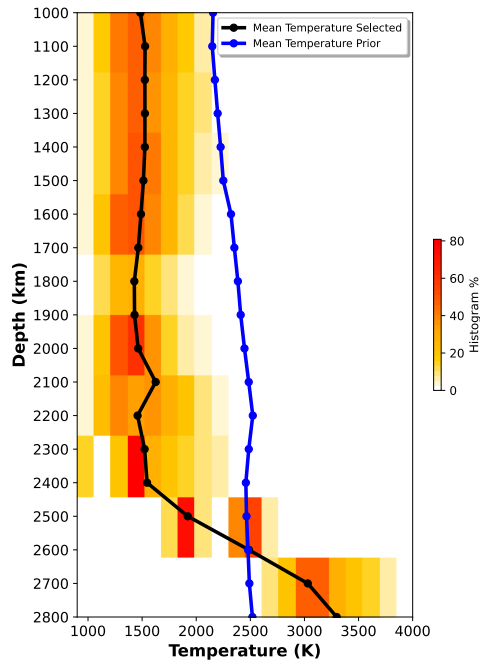
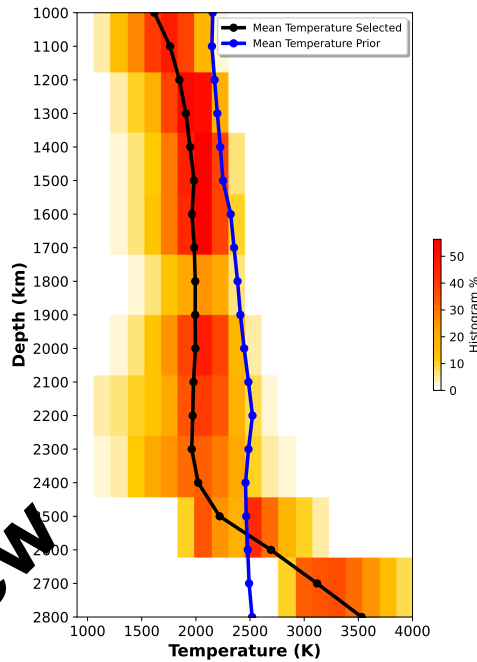


Figure 4.3: Adiabatic Temperature Profile in the Earth mantle constructed with data from (Katsura, 2022, Table 3)

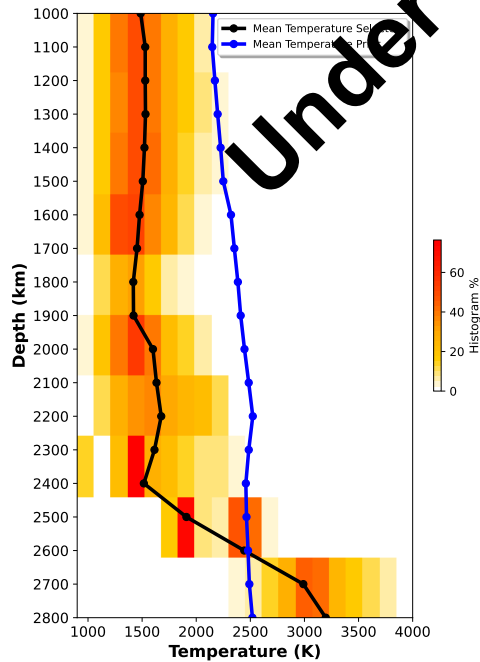
Moreover, some research suggests that homogeneous aggregates with ferropericlase (Fp) might also exhibit an anticorrelation between shear velocity and bulk sound velocity. Other researchers have shown from the solidus of mantle rocks using high-pressure experiments and three-dimensional x-ray microtomographic imaging, that the solidus temperature of a pyrolitic mantle could be established around $3570 \pm 200\text{K}$ at pressures of the CMB (Nomura et al., 2014). Accordingly, it would be possible for post-perovskite phase to exist in wide areas of the lowermost mantle. Other researchers have examined lateral variations in seismic shear wave velocity and in attenuation. This has shown to be a good way to constrain the thermochemical properties of the lowermost mantle. Since the velocity of shear waves is affected by the presence of post-perovskite (pPv) and the stability of pPv is highly temperature-dependent, determining the right amounts of it and its effect on shear velocity would help to determine the local and average horizontal temperature in the lowermost mantle, estimating a temperature at the CMB at the Northern Pacific of 3470–3880 K with a 95% likelihood (Deschamps & Cobden, 2022).



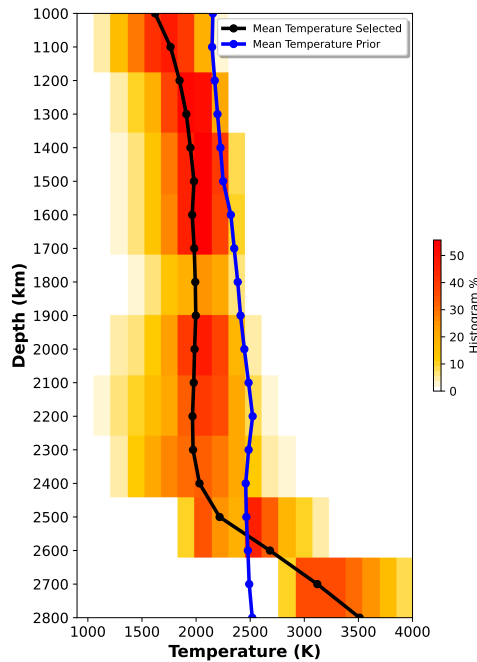
(a) Temperature distribution for GLAD-M25 without ISC



(b) Temperature distribution for GLAD-M25 with ISC



(c) Temperature distribution for GLAD-M35 without ISC



(d) Temperature distribution for GLAD-M35 with ISC

Figure 4.4: Temperature Distribution as function of depth with and without ISC for GLAD-M25 and GLAD-M35.

Silica content also shows a more realistic behavior when ISC is incorporated. Previous studies have shown that the lower mantle is constituted by 93% of its volume in bridgemanite (Murakami et al., 2012, Abstract). This enrichment can be seen when added the ISC, leading to more plausible results.

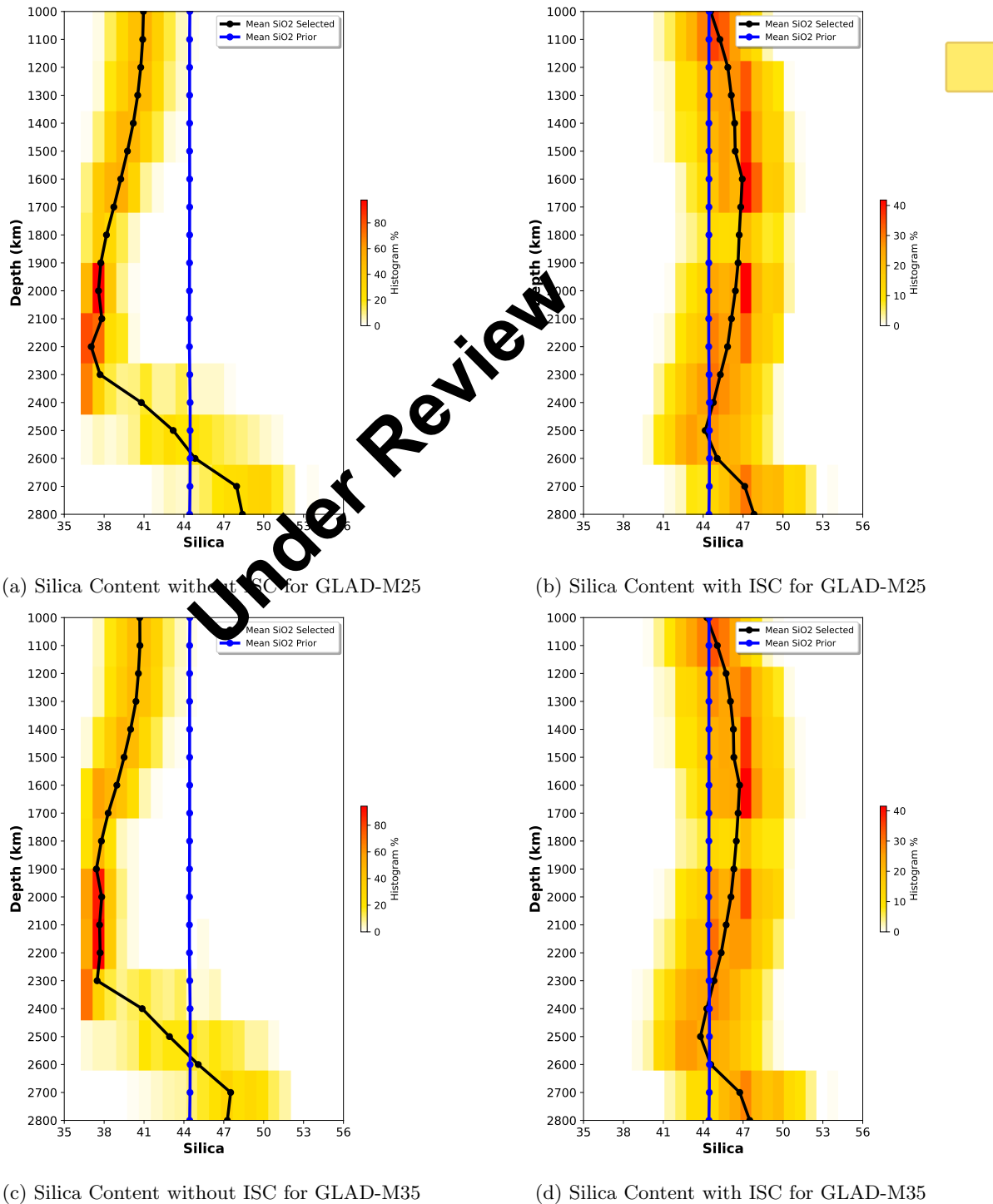


Figure 4.5: Silica distribution as function of depth for Prior with and without ISC for GLAD-M25 and GLAD-M35.

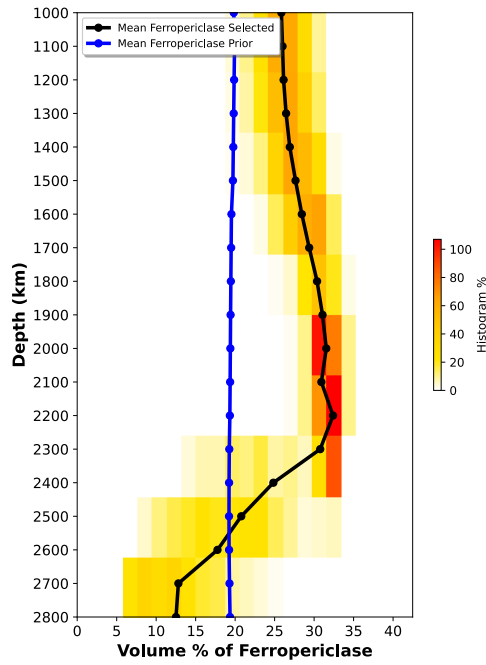
Nowadays, it is largely agreed that chemical heterogeneity is needed to explain the shear and bulk wave speeds in the lower mantle (Su & Dziewonski, 1997). However, the ratio from compressional and shear wave is not useful to discern between iron anomalies and pure temperature anomalies with depth (Trampert et al., 2004). The ratio $R_{\Phi} = \frac{\delta \log V_{\Phi}}{\delta \log V_s}$ is shown to be negative in the lower mantle giving the best an indication of the presence of chemical heterogeneity, in particular in the bottom of the lower mantle, where significant anelastic effects and chemical heterogeneity is argued (Karato & Karki, 2001).

In order to vary the elastic moduli resulting in chemical variations, Fe can vary inside a chemical heterogeneous rock or to the Si/Fe ratio-(ratio of bridgmanite to ferropericlase). Moreover, other studies pointed out that the anticorrelation between shear velocity and bulk sound velocity may also be produced in homogeneous aggregates containing ferropericlase (Fp) (Wu & Wentzcovitch, 2014, Abstract). As mentioned in the proceeding section, Fp is the second most abundant mineral phase in the lower mantle, so discerning its physical properties has a large relevance. Assessing if ISC happens for ferropericlase in the mantle is important since it has been reported that the influence in softening the bulk modulus can cause major changes relevant for large-scale geophysical properties (Trautner et al., 2023). Ferropericlase contains around 20% of Fe^{2+} and not more than 1% of Fe^{3+} .

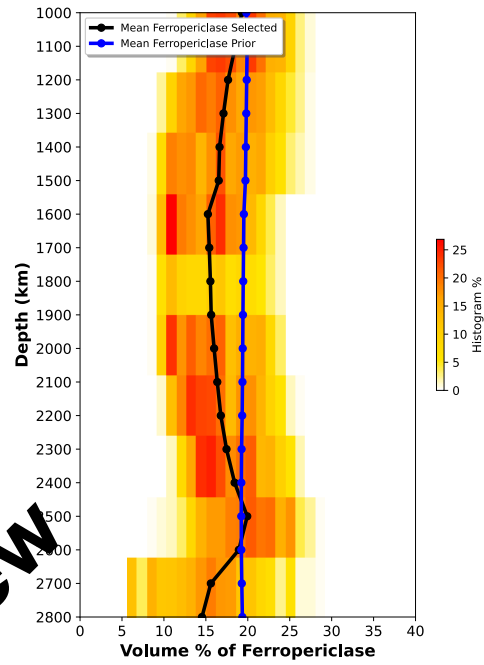
The transition from bridgmanite (Pv) to post-perovskite (pPv) has been known for already 20 years when different researchers showed that the polymorphic transformation from bridgmanite into pPv near the CMB was possible (Murakami et al., 2004). Interpreting the effect of ISC on Pv and pPv is challenging because of the varying valence states and site occupancy in both Fe phases (Lin et al., 2013).

Determining the right amount of pPv in the lower mantle is crucial for establishing the convective evolution of the lower mantle. Earth dynamics and evolution may differ when not including the precise amount of pPv, affecting for instance the sinking slabs in the mantle as showed by Nakagawa and Tackley (2011) among other researchers. Moreover, constraining post-perovskite will help to establish better the degree of chemical heterogeneity in the D'' region, which has a key importance in roles as the amount of heat leaving Earth's core.

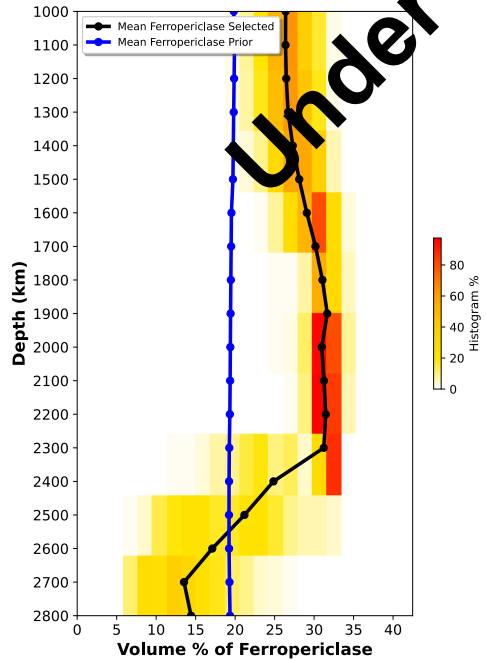
Next 3 figures (4.6, 4.7 and 4.8) show the distribution of these different minerals in the lower mantle. Incorporating the ISC on the lower mantle, ferropericlase shows between 10% and 20% in volume as expected from theoretical calculations. Interestingly, without this quantum effect, the algorithm selected unrealistic ferropericlase amounts around 2200 km depth, where the ISC is present. In other words, the thermochemical models contained more ferropericlase than theoretically calculated in order to fit the velocities in the STZ. Bridgmanite shows a distribution around 70-80% over the whole lower mantle. Finally, the MH algorithm selected large proportions of post-perovskite on the lowermost mantle. Models selected to fit both tomographic target values show very similar results, being consistent with each other.



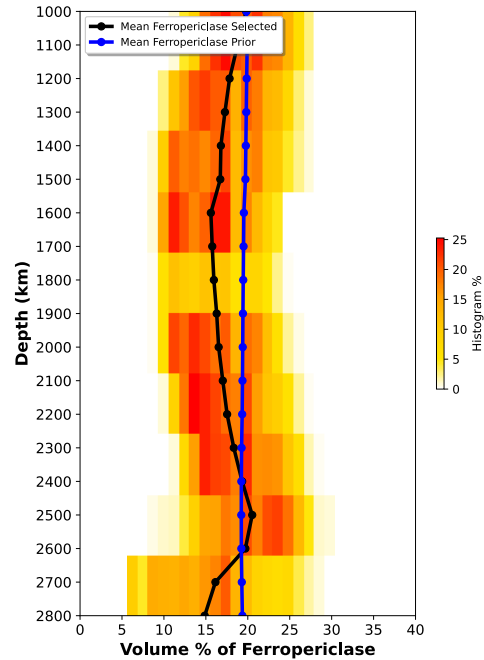
(a) Ferropericlase distribution for Prior without ISC for GLAD-M25



(b) Ferropericlase distribution for Prior with ISC for GLAD-M25



(c) Ferropericlase distribution for Prior without ISC for GLAD-M35



(d) Ferropericlase distribution for Prior with ISC for GLAD-M35

Figure 4.6: Ferropericlase distribution as a function of depth for Prior with and without ISC for GLAD-M25 and GLAD-M35.

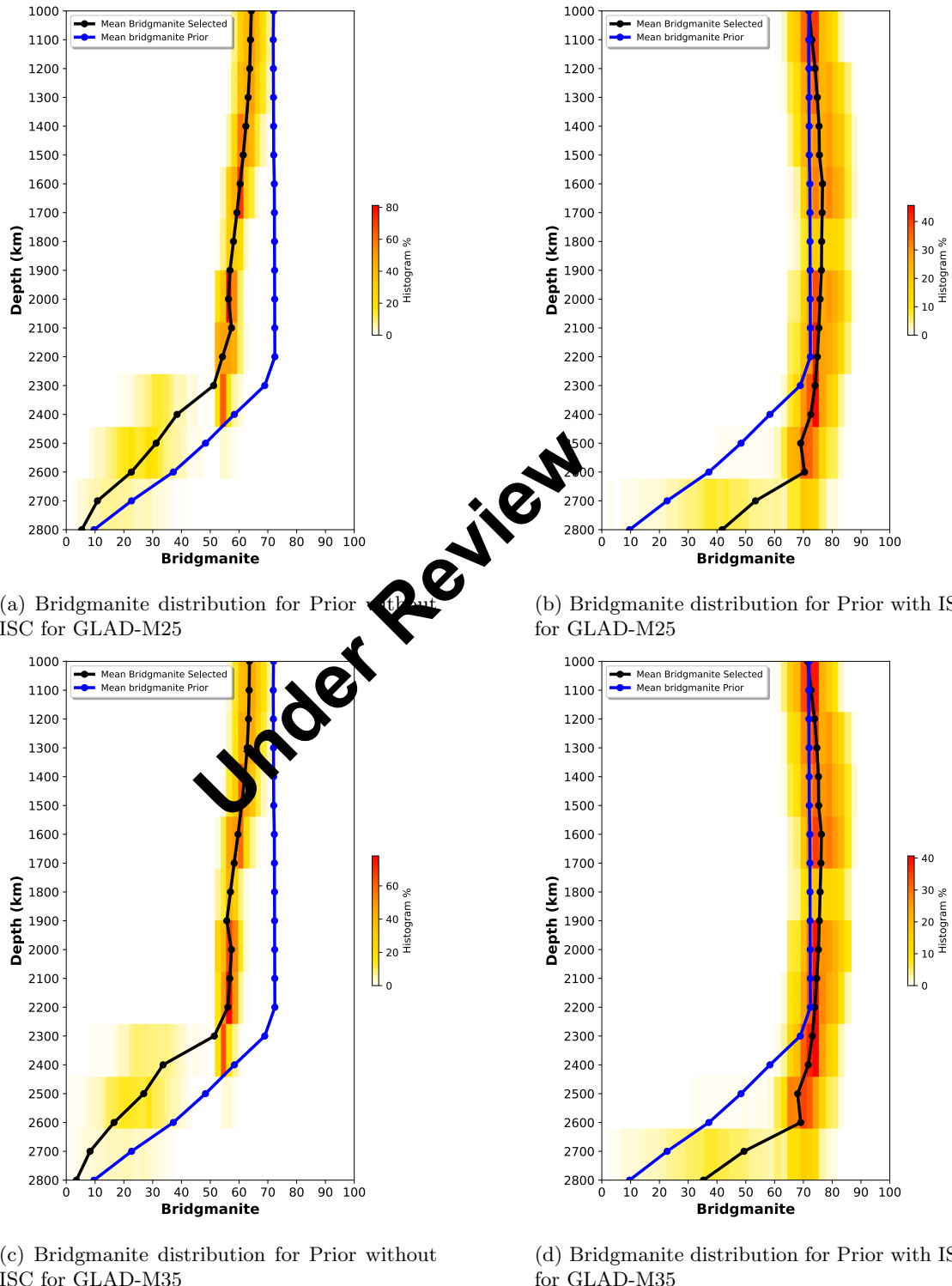


Figure 4.7: Bridgmanite distribution as function of depth for Prior with and without ISC for GLAD-M25 and GLAD-M35.

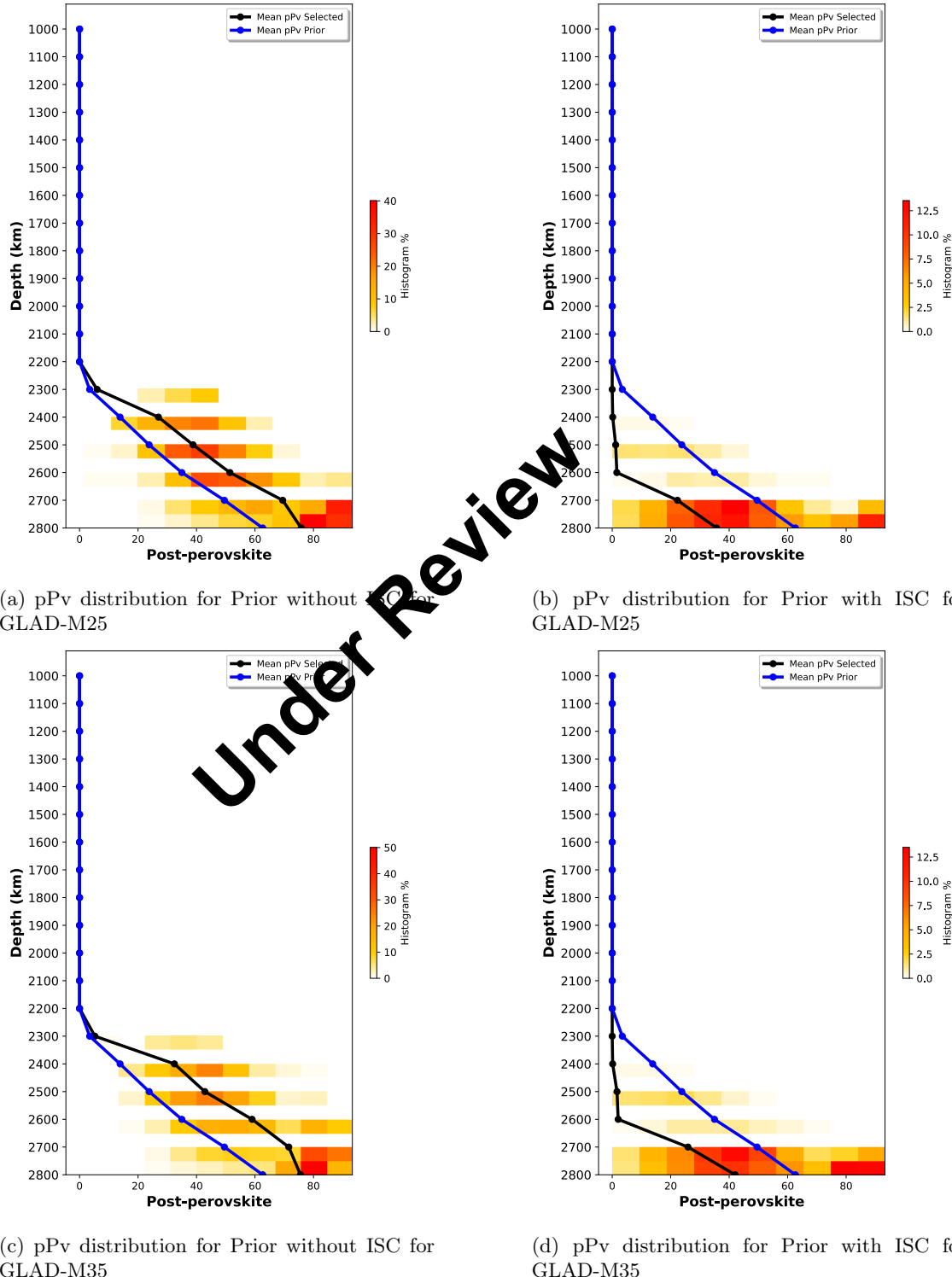


Figure 4.8: Post-perovskite distribution as function of depth for different prior with and without ISC for GLAD-M25 and GLAD-M35.

Finally, the next two figures 4.9 and 4.10 show the amount of MgO and FeO compounds on the lower mantle. The interior of Earth is rich in magnesium, oxygen, and iron so these minerals are good models for studying the nature of planetary interiors. For instance, ferropericlase contains both magnesium and iron oxide so determining the right content is important. FeO plays a crucial role in regulating the properties and evolution of the interior of Earth. As an example of the importance of these elements, establishing the melting point of FeO in the series $FeO - MgO - SiO_2$ of the mantle is crucial since it has the main role of controlling the crystallization sequence of Earth's primordial magma ocean (Dobrosavljevic et al., 2023). Furthermore, establishing the accurate properties of FeO at the D'' region is also significant in the context of ultra low velocity zones (ULVZ), where the seismic wave speeds are drastically reduced showing an Earth's heterogeneous mantle base (Garnero & Helmberger, 1998). These structures are found at the boundaries of large thermochemical piles and are believed to be the origins of significant mantle plumes that give rise to volcanic hotspots (McNamara et al., 2010) (French & Romanowicz, 2015).

Dobrosavljevic et al. (2023) have shown that FeO in the lower mantle stays in solid structures. This indicates that a ULVZ containing solid FeO could likely have greater bulk electrical and thermal conductivity compared to the surrounding mantle (Manga & Jeanloz, 1996). Again, the results for the new tomography model are consistent with the former tomography model.

Under Review

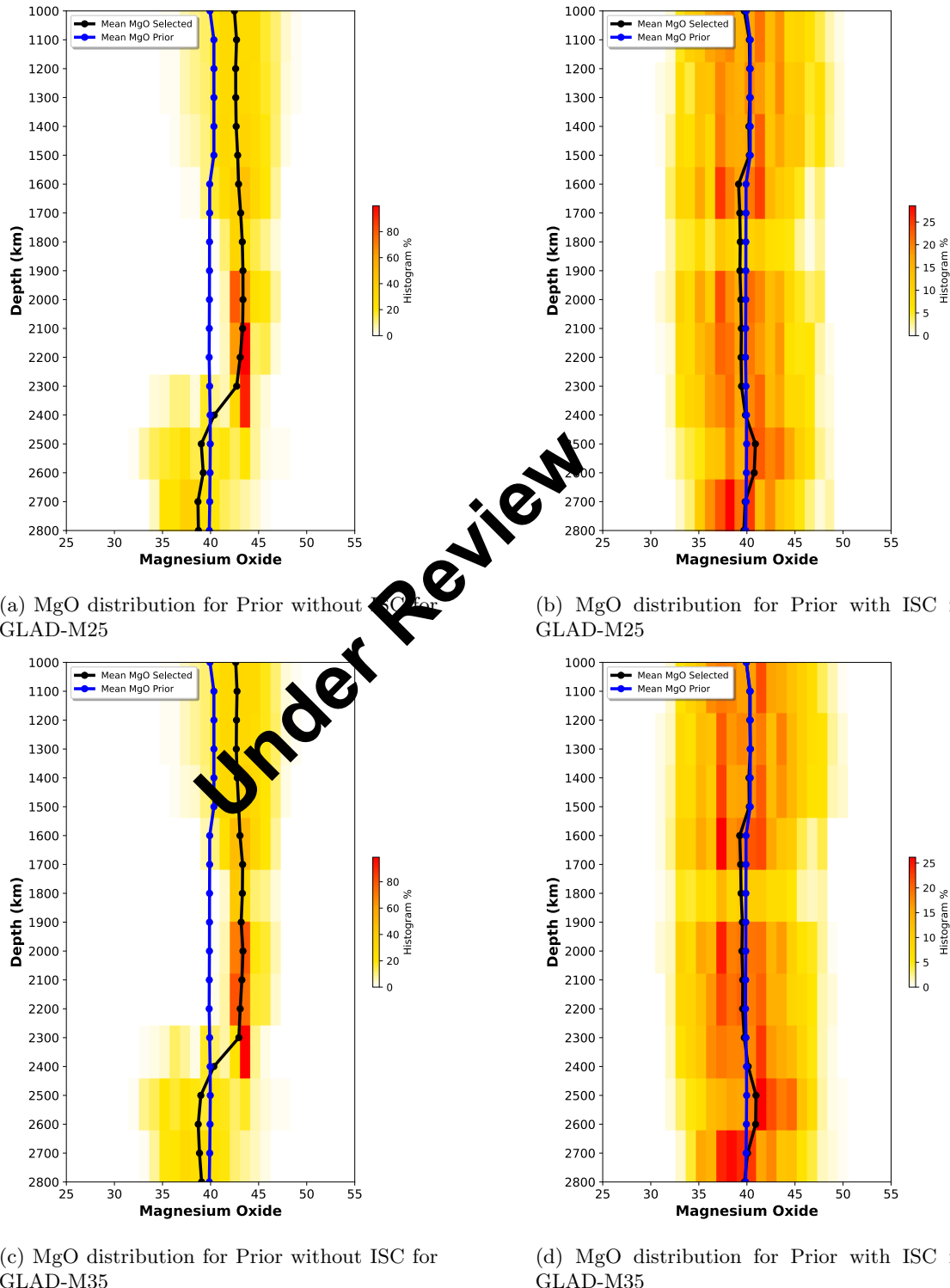


Figure 4.9: MgO distribution as function of depth for Prior with and without ISC for GLAD-M25 and GLAD-M35

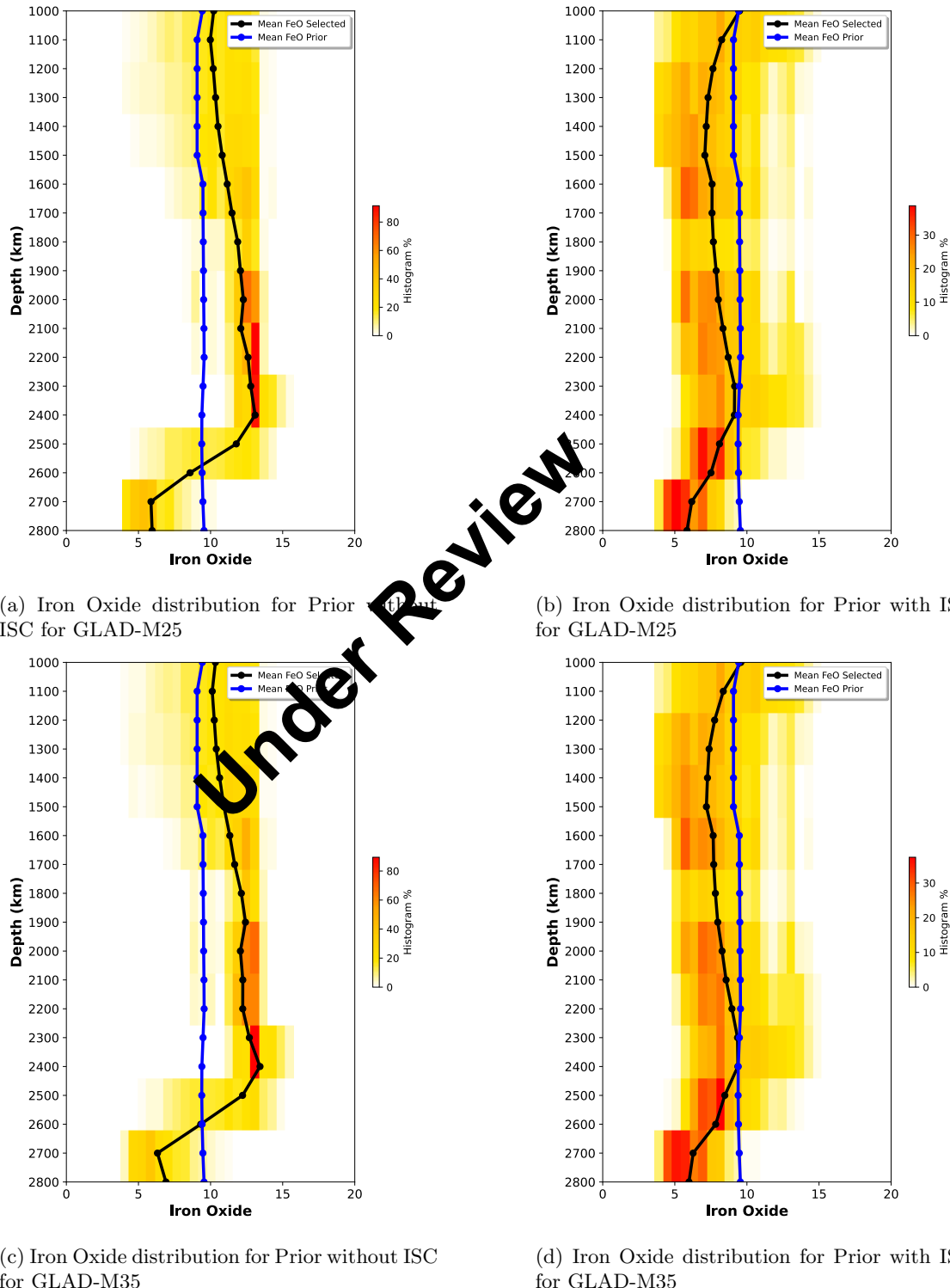


Figure 4.10: Iron Oxide distribution as a function of depth for Prior with and without ISC for GLAD-M25 and GLAD-M35.

4.2 Broad Prior

The composition of the lowermost mantle is still not well resolved today. Variations in lower mantle composition can lead to significant differences in its rheological properties. The presence of SiO_2 -enriched rocks in the lower mantle has been suggested to balance the Earth's silica budget concerning chondrites, especially considering the limited capacity to dissolve silica in the current outer core (Ballmer et al., 2017).

Moreover, other studies have considered the presence of a basal magma ocean in the early history of the planet. Now, fractionated remnants of an ancient magma ocean could be responsible for the enrichment in silica (Labrosse et al., 2007).

In the previous section, the Restricted chemical Prior cannot fit the seismic velocities from 2600 km depth to the CMB. In order to study if velocities can be fitted, we now use the Broader chemical Prior that includes a wider range of chemical models. Now, using this new chemical broad prior, we get a larger number of accepted values for the lowermost mantle 4.11. This selected prior models are able to fit the target tomographic velocities for the D'' region. Figure 4.13 shows the distribution of silica for the lower mantle. Interestingly, it can be seen how around a 7% more silica is selected for the D'' region than for the Restricted Prior.

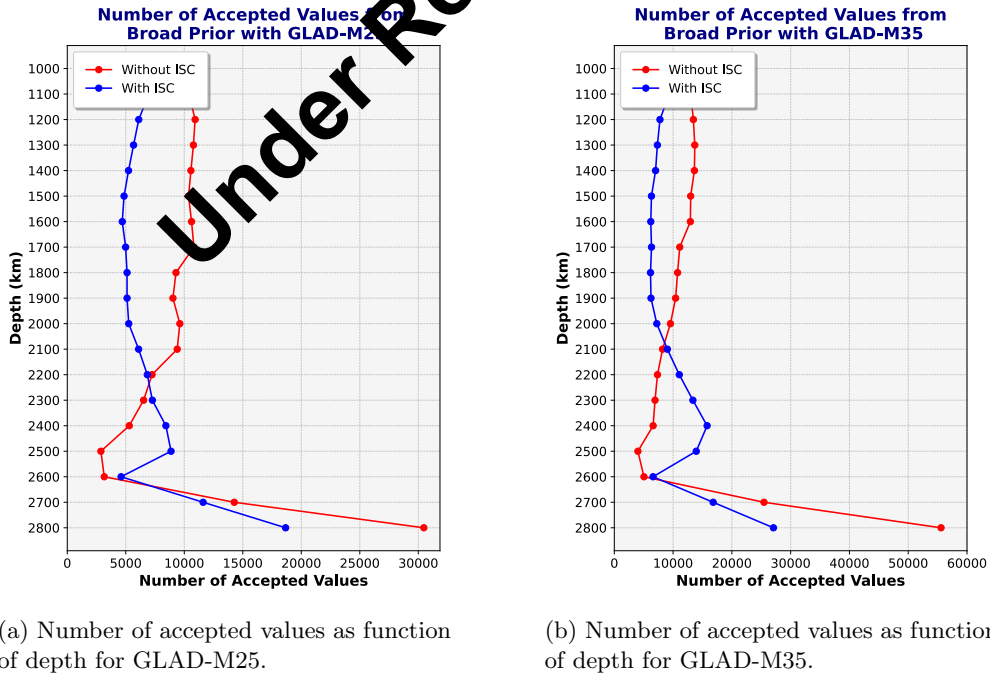


Figure 4.11: Accepted values for GLAD-M25 and GLAD-M35 for Broad Prior.

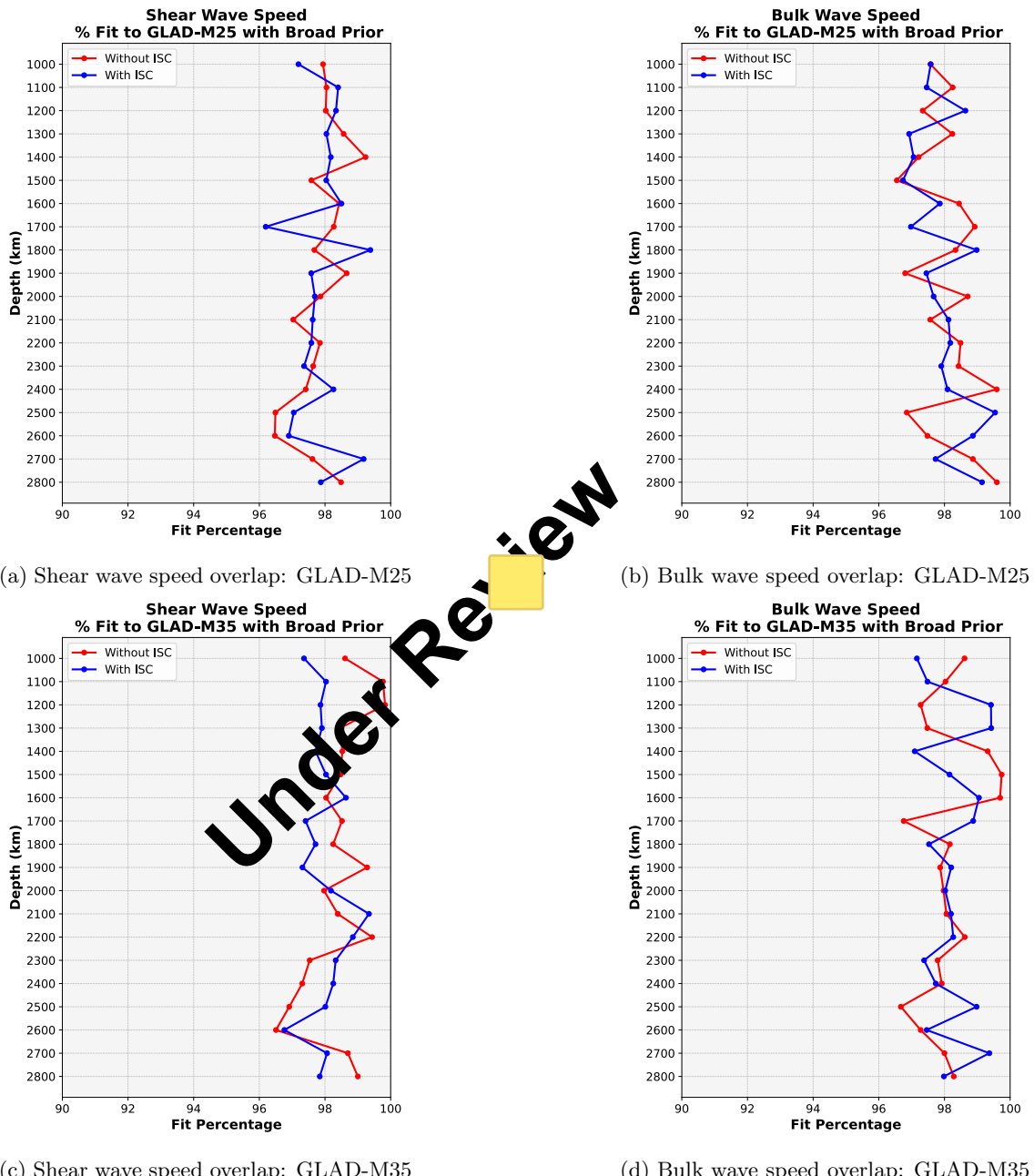


Figure 4.12: Bulk and Shear wave speeds fit with and without Iron Spin Crossover in Broad Prior for GLAD-M35 and GLAD-M25.

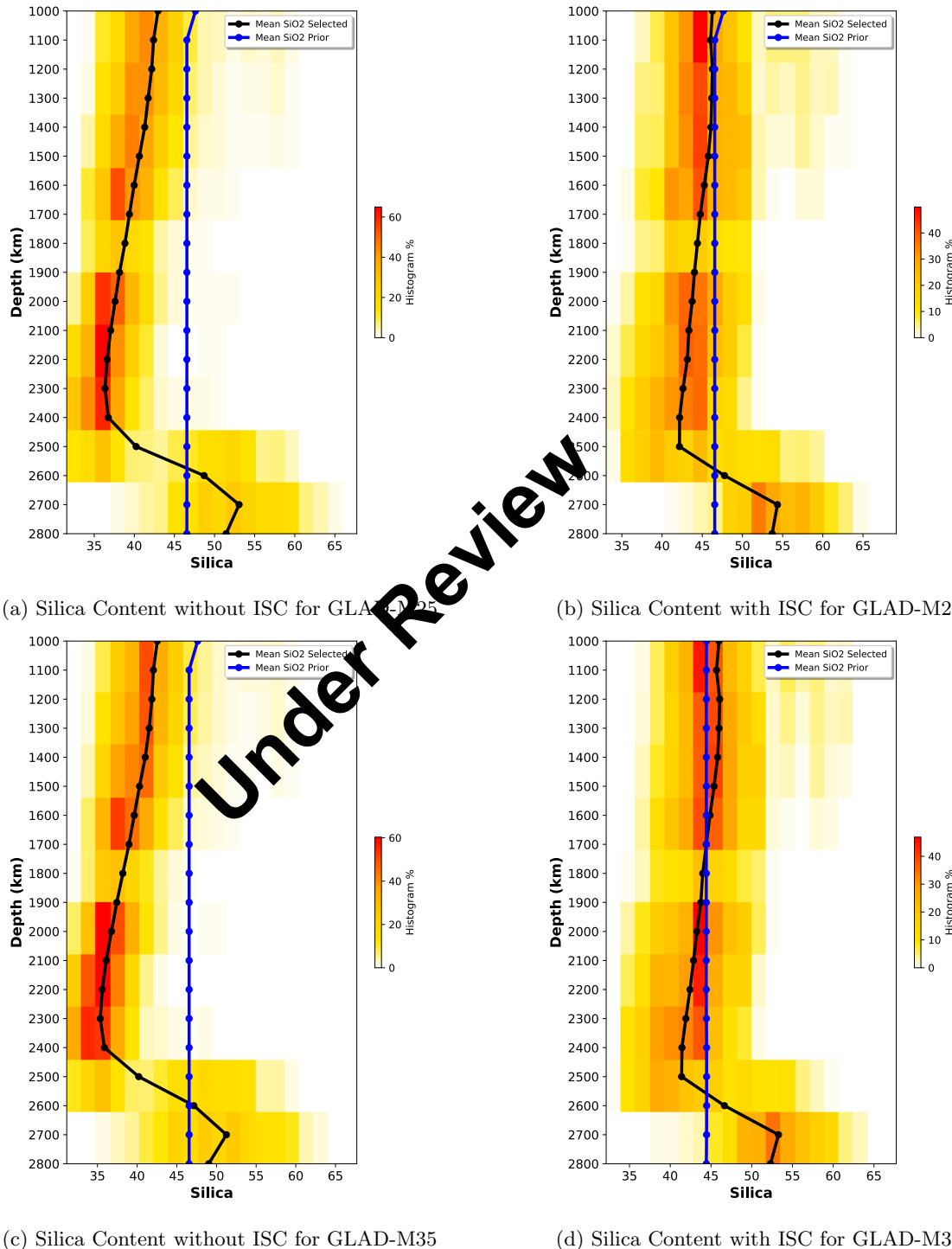


Figure 4.13: Silica distribution as function of depth for Prior with and without ISC for GLAD-M25 and GLAD-M35.

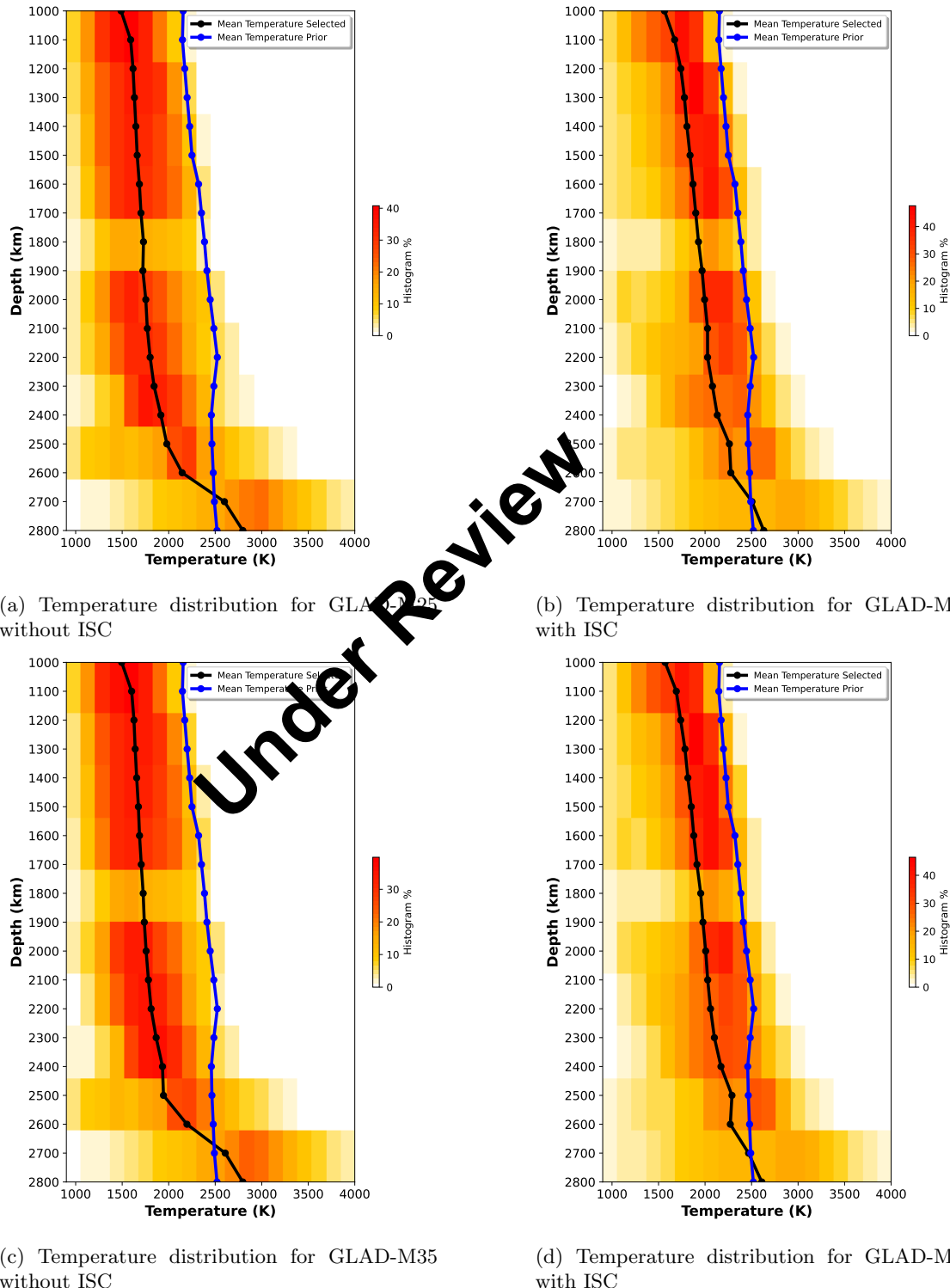


Figure 4.14: Temperature Distribution as a function of depth with and without ISC for GLAD-M25 and GLAD-M35.

4.3 Results Summary

This section summarizes the various thermochemical results selected from the Prior models. One can compare the mineralogical distributions that fit the observed wave speeds of both GLAD-M25 and GLAD-M35 full waveform tomography models. The results from these two models show no significant differences. Both models demonstrate an improved fit when the ISC is included. Furthermore, the inclusion of the ISC aligns our results with theoretical mantle models from other studies. Ferropericlase consists of between 15% - 20% of the lower mantle, bridgemanite represents between 70% and 80% and pPv is represented only in the lowermost mantle.

To fit the seismic velocities in the lowermost mantle with the ISC, an extra enrichment in silica is required compared to the upper mantle. Theoretical observations support this silica enrichment due to compositional variations. Previous studies have shown an enrichment quantified around 20% in silica on an atomic basis ($Mg/Si = 1.1$) for the lower mantle relative to the upper mantle (Mashino et al., 2020). This enrichment is also in agreement with seismic tomography images of stagnant slabs at 1000 km (Ballmer et al., 2015). Moreover, inefficient mixing throughout Earth's history may have prevented complete homogenization of the lower mantle, leaving remnants of an ancient magma ocean and anomalous low shear velocity zones.

The following table (4.1) presents the values for different depths for easy data reference. The data are taken from the results of models selected from both the Restricted Prior and Broad Prior, with the latter highlighted by the symbol *.

Best Thermochemical Results					
Depth (km)	% Fit v_Φ	% Fit v_s	T \pm 100 (K)	Si \pm 1%	Fp \pm 1%
1000	98.7%	98.9%	1600	44.5	20
1400	99.5%	99.2%	1950	46	16.5
1800	97.4%	98.1%	2000	46.5	16
2200	98.8%	98.2%	1975	45	17.5
2600	97.4%	96.8%	2650	44.5	20
2800	97.4%*	96.8%*	3500	48*	15

Best Thermochemical Results				
Depth (km)	Pv \pm 2%	pPv \pm 5%	MgO \pm 1%	FeO \pm 1%
1000	72	0	40	9
1400	76	0	40.5	7.5
1800	77	0	39.5	7
2200	75	0	39.5	9
2600	70	1	41	7.5
2800	35	38	40	6

Table 4.1: Thermochemical models for 6 different lower mantle depths.

Chapter 5

Discussion

This study aimed to enhance our understanding of the lower mantle's thermochemical properties using the GLAD-M35 full-waveform tomography model. This was accomplished by performing a joint bulk and shear wave speeds treatment with absolute velocities. Specifically, first, we wanted to reproduce the results from Cobden et al. (2024) using the same tomography model GLAD-M25 that they used in their work. Next, using the new GLAD-M35 tomography model (Cui et al., 2024) and the same thermochemical prior models used in (Cobden et al., 2024), the goal was to examine if the models containing the ISC in ferropericlase were able to fit the target wave speeds. Finally, the selected thermochemical models are plotted for further study.

The methodology involved using two sets of prior models (Restricted and Broad) to fit the observed shear and bulk wave velocities from the GLAD-M25 and GLAD-M35 tomography models. The Metropolis-Hastings algorithm was employed to iteratively select the models that best matched the observed data. As mentioned in the preceding sections, the results showed a significant improvement in the fit when the ISC was included, highlighting the importance of this quantum effect in explaining the seismic properties of the lower mantle. The number of accepted values was significantly higher with ISC, indicating that the prior models without ISC were insufficient to explain the observed seismic velocities at depths between 1800 and 2700 km. Without ISC, the temperature estimates were unrealistically low, so the importance of ISC in accurately modeling the mantle's thermal state has been proven.

Furthermore, the inclusion of this quantum effect led to more plausible distributions of the different minerals like ferropericlase and bridgmanite. The unrealistic amounts of ferropericlase in models without ISC, particularly around 2200 km depth, were corrected when ISC was included, suggesting that ISC is crucial for accurate mineralogical modeling. Nonetheless, due to the fact of using bulk wave instead of P-wave and absolute wave speed dismisses the argumentation that the velocity wave anomalies could be explained by a SiO_2 enrichment. Furthermore, variations in different chemical amounts are unlikely to cause the same effect in the results since the uncertainties would cause a similar effect at all depths. In this study, it is shown how the anomalous seismic wave region is not spread over the whole data type but constrained in specific depths.

As also shown in (Cobden et al., 2024) anelasticity effects cannot explain the results, since anelasticity would decrease the v_s relative to the v_Φ , while the new tomographic data requires the opposite effect.

Despite the robust findings, the study may present some limitations such as the prior models used might still have inherent assumptions and simplifications that do not capture all complexities of the mantle. Also, although 19 depths in steps of 100 km were considered, the resolution might not capture finer-scale variations in seismic properties. Alternative modeling approaches would

strengthen the findings such as comparing normal mode data and studying the iron spin crossover in bridgmanite and post-perovskite.

As mentioned before, the elastic properties derived from the inclusion of ISC in ferropericlase and bridgmanite certainly causes a large impact in the dynamics of the lower mantle. The softening of the bulk modulus would cause anomalies in the thermoelastic properties of Fe and Mg (Wentzcovitch et al., 2009). Furthermore, constraining this effect is also important to understand the present state of heat exchange with the core or the evolution of thermochemical structures such as LLSVP or ULVZ. Recent studies propose that the large structures in the lower mantle, once believed to be composed of partial melt, can now be attributed to solid $(Mg, Fe)O$ with high FeO concentrations (Dobrosavljevic et al., 2023). Accurately determining the amount of FeO with ISC is therefore crucial. Establishing the correct thermochemical parameters of the lower mantle is essential for understanding its current state and for performing precise thermochemical simulations of the planet's interior evolution.

The results in this study validated the hypothesis that ISC must be considered to reconcile the seismic data with theoretical models. The evidence here robustly supports the ISC's effect, thus addressing the research questions effectively.

Under Review

Chapter 6

Conclusion

The goal of this thesis was to corroborate if the Iron Spin Crossover in ferropericlase was visible using the new GLAD-M35 full-waveform tomography model. By incorporating the iron spin crossover (ISC) effect in ferropericlase, we wanted to determine whether this quantum effect could match observed seismic velocities with theoretical models. The research effectively addressed this aim and furthermore, once the appropriate models for the mantle were selected, new substantial insights into the mantle's compositional and thermal state were provided.

The results unequivocally demonstrate that the ISC effect is crucial for accurately fitting the observed mantle sound wave speeds and to accurately model the mantle's properties. The inclusion of ISC consistently resulted in better fits across both the GLAD-M25 and GLAD-M35 tomography models, specifically at depths where the previous theoretical works pointed out the presence of the ISC, confirming the hypothesis that ISC plays a significant role in explaining the observed seismic properties.

Although the Restricted Prior could fit almost the entire lower mantle, [chemical heterogeneity](#) was needed to fit the lowermost part of the mantle. The silica enrichment could reconcile the theory of a primordial basal magma ocean, MORB accumulation on the D'' region and observations of chondritic meteorites.

The consistent improvement in fit with the inclusion of ISC data significantly diminishes the plausibility of alternative explanations, particularly given the consistency and robustness of these results across various depths and models. This finding not only validates the current methodology but also opens up promising avenues for future research aimed at refining our understanding of the Earth's mantle. Future research should delve into the geographical variability of the enriched models, utilizing 3D absolute wave speeds to uncover regional differences. Additionally, there is a need to focus on the role of Fe^{3+} in bridgmanite and post-perovskite phases. Investigating these aspects could provide critical insights into the composition and behavior of the lower mantle, leading to more accurate and detailed models. Such refined models would not only enhance our theoretical knowledge of the mantle but could also have practical implications for understanding the geodynamic processes and the Earth's evolution.

Appendix A

Appendix

Under Review

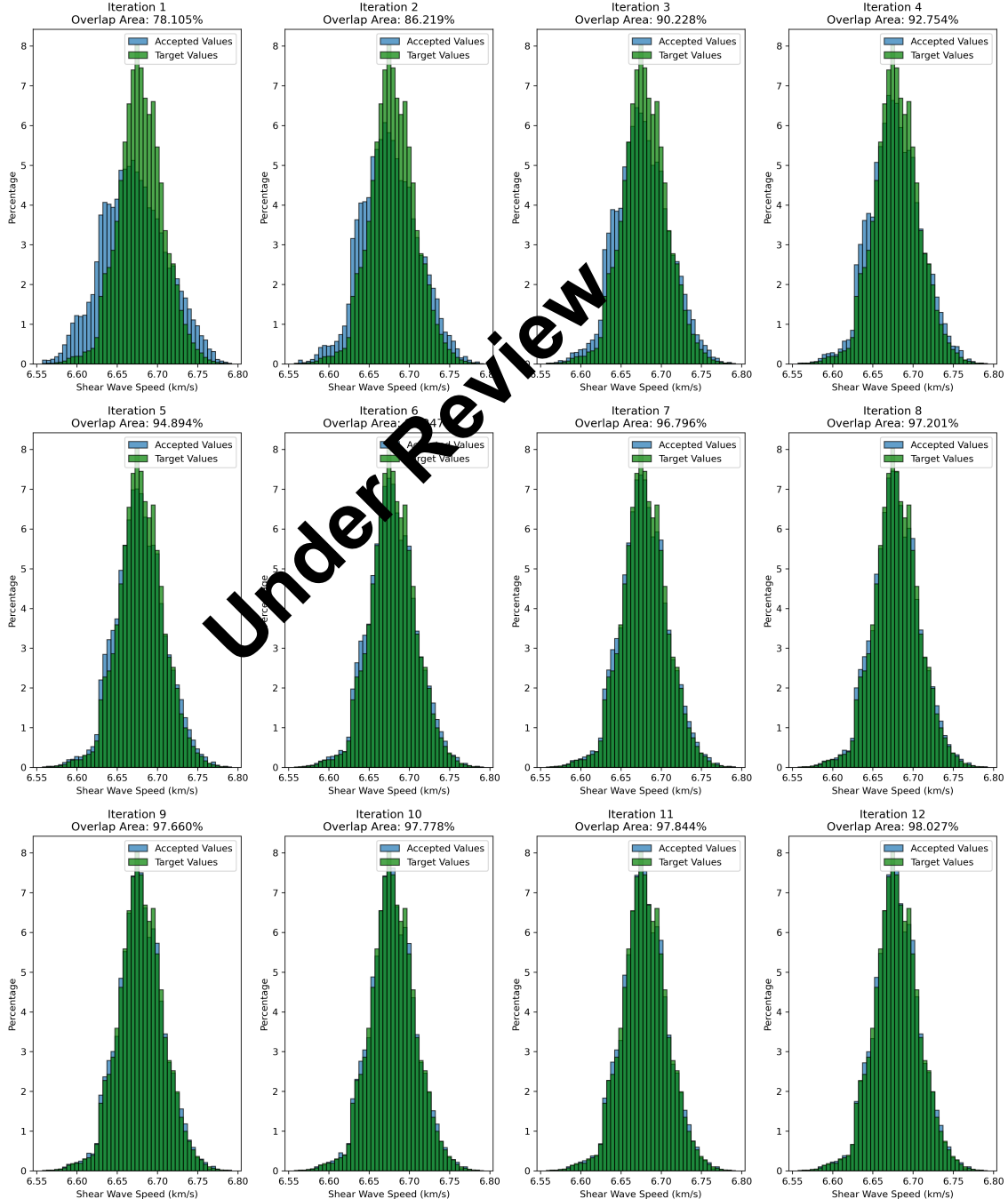


Figure A.1: Histograms showing the iterative fitting process on histograms for shear wave values at 1500km depth in GLAD-M35.

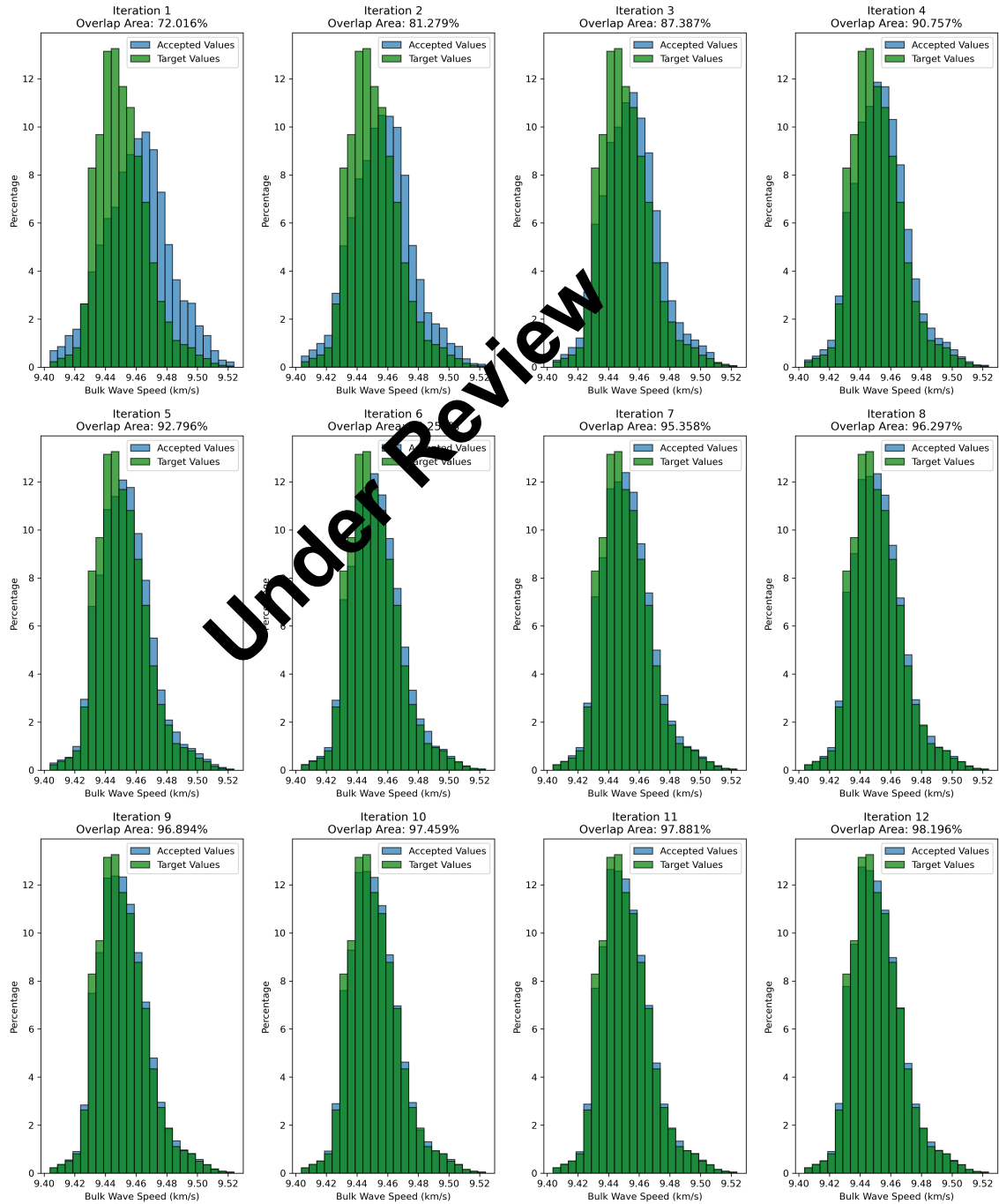
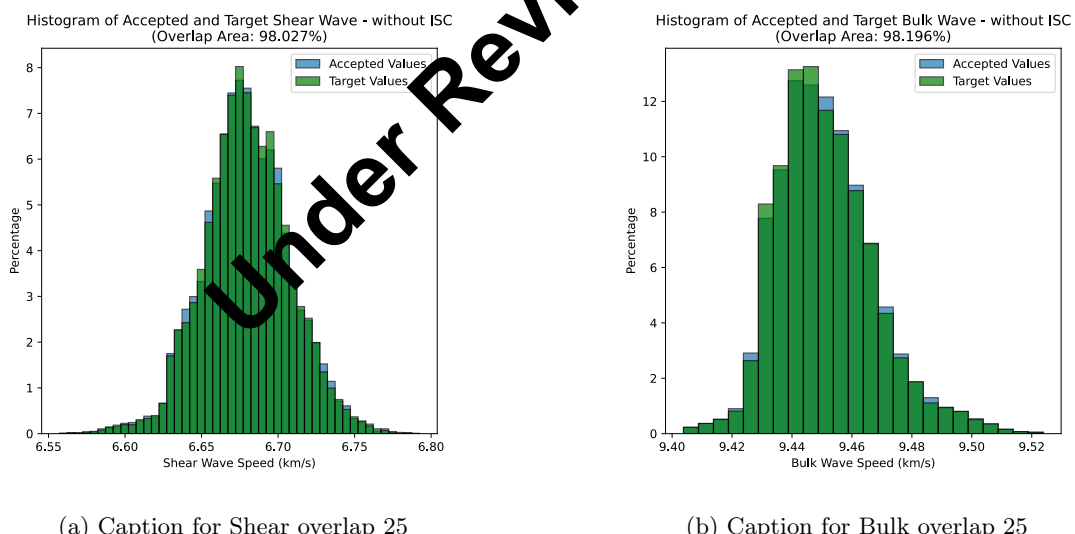


Figure A.2: Histograms showing the iterative fitting process on histograms for bulk wave values at 1500km depth in GLAD-M35.



(a) Caption for Shear overlap 25

(b) Caption for Bulk overlap 25

Figure A.3: Final Accepted histograms for the joint inverted Shear and Bulk waves at 1500km depth without ISC present on the Prior model for GLAD-M35.

Bibliography

- Afonso, J. C., Fullea, J., Griffin, W. L., Yang, Y., Jones, A. G., Connolly, J. A. D., & O'Reilly, S. Y. (2013). 3-D multiobservable probabilistic inversion for the compositional and thermal structure of the lithosphere and upper mantle. I: a priori petrological information and geophysical observables. *Journal of geophysical research. Solid earth*, 118(5), 2586–2617. <https://doi.org/10.1002/jgrb.50124>
- Badro, J., Fiquet, G., Guyot, F., Rueff, J.-P., Sverján, V. V., Vanko, G., & Monaco, G. (2003). Iron partitioning in Earth's mantle: toward a deep lower mantle discontinuity. *Science*, 300(5620), 789–791. <https://doi.org/10.1126/science.1081311>
- Badro, J., Rueff, J.-P., Vanko, G., Monaco, G., Fiquet, G., & Guyot, F. (2004). Electronic transitions in perovskite: possible nonconvecting layers in the lower mantle. *Science*, 305(5682), 383–386. <https://doi.org/10.1126/science.1098840>
- Ballmer, M. D., Houser, C., Hernlund, J. W., Wentzcovitch, R. M., & Hirose, K. (2017). Persistence of strong silica-enriched domains in the Earth's lower mantle. *Nature geoscience*, 10(3), 236–240. <https://doi.org/10.1038/ngeo2898>
- Ballmer, M. D., Schmerr, N. C., Nakagawa, T., & Ritsema, J. (2015). Compositional mantle layering revealed by slab stagnation at 1000-km depth. *Science advances*, 1(11). <https://doi.org/10.1126/sciadv.1500815>
- Cobden, L., Mosca, I., Trampert, J., & Ritsema, J. (2012). On the likelihood of post-perovskite near the core–mantle boundary: A statistical interpretation of seismic observations. *Physics of the earth and planetary interiors*, 210–211, 21–35. <https://doi.org/10.1016/j.pepi.2012.08.007>
- Cobden, L., Zhuang, J., Lei, W., Wentzcovitch, R., Trampert, J., & Tromp, J. (2024). Full-waveform tomography reveals iron spin crossover in Earth's lower mantle. *Nature communications*, 15(1). <https://doi.org/10.1038/s41467-024-46040-1>
- Cohen, R. E., Mazin, I. I., & Isaak, D. G. (1997). Magnetic collapse in transition Metal oxides at High pressure: Implications for the Earth. *Science*, 275(5300), 654–657. <https://doi.org/10.1126/science.275.5300.654>
- Cui, C., Lei, W., Liu, Q., Peter, D., Bozdağ, E., Tromp, J., Hill, J., Podhorszki, N., & Pugmire, D. (2024). GLAD-M35: A joint P and S global tomographic model with uncertainty quantification [Submitted]. *Geophys. J. Int.*
- Deschamps, F., & Cobden, L. (2022). Estimating core-mantle boundary temperature from seismic shear velocity and attenuation. *Frontiers in earth science*, 10. <https://doi.org/10.3389/feart.2022.1031507>
- Deschamps, F., Cobden, L., & Tackley, P. J. (2012). The primitive nature of large low shear-wave velocity provinces. *Earth and planetary science letters*, 349–350, 198–208. <https://doi.org/10.1016/j.epsl.2012.07.012>

- Deschamps, F., & Trampert, J. (2003). Mantle tomography and its relation to temperature and composition. *Physics of the earth and planetary interiors*, 140(4), 277–291. <https://doi.org/10.1016/j.pepi.2003.09.004>
- Dobrosavljevic, V. V., Zhang, D., Sturhahn, W., Chariton, S., Prakapenka, V. B., Zhao, J., Toellner, T. S., Pardo, O. S., & Jackson, J. M. (2023). Melting and defect transitions in FeO up to pressures of Earth's core-mantle boundary. *Nature communications*, 14(1). <https://doi.org/10.1038/s41467-023-43154-w>
- Fichtner, A. (2021, July). *Lecture notes on inverse theory*. <https://doi.org/10.33774/coe-2021-qpq2j>
- French, S. W., & Romanowicz, B. (2015). Broad plumes rooted at the base of the Earth's mantle beneath major hotspots. *Nature*, 525(7567), 95–99. <https://doi.org/10.1038/nature14876>
- Garnero, E. J., & Helmberger, D. V. (1998). Further structural constraints and uncertainties of a thin laterally varying ultralow-velocity layer at the base of the mantle. *Journal of geophysical research*, 103(B6), 12495–12509. <https://doi.org/10.1029/98jb00700>
- Karato, S.-i., & Karki, B. B. (2001). Origin of lateral variation of seismic wave velocities and density in the deep mantle. *Journal of geophysical research*, 106(B10), 21771–21783. <https://doi.org/10.1029/2001jb000214>
- Katsura, T. (2022). A revised adiabatic temperature profile for the mantle. *Journal of geophysical research. Solid earth*, 127(2). <https://doi.org/10.1029/2021jb023562>
- Labrosse, S., Hernlund, J. W., & Cottine, N. (2007). A crystallizing dense magma ocean at the base of the Earth's mantle. *Nature*, 450(7171), 866–869. <https://doi.org/10.1038/nature06355>
- Lin, J.-F., Speziale, S., Mao, Z., & Marquardt, H. (2013). EFFECTS OF THE ELECTRONIC SPIN TRANSITIONS OF IRON IN LOWER MANTLE MINERALS: IMPLICATIONS FOR DEEP MANTLE GEOPHYSICS AND GEOCHEMISTRY. *Reviews of geophysics*, 51(2), 244–275. <https://doi.org/10.1002/rog.20010>
- Lin, J.-F., Vanko, G., Jacobsen, S. D., Iota, V., Struzhkin, V. V., Prakapenka, V. B., Kuznetsov, A., & Yoo, C.-S. (2007). Spin transition zone in Earth's lower mantle. *Science*, 317(5845), 1740–1743. <https://doi.org/10.1126/science.1144997>
- Manga, M., & Jeanloz, R. (1996). Implications of a metal-bearing chemical boundary layer in D for mantle dynamics. *Geophysical research letters*, 23(22), 3091–3094. <https://doi.org/10.1029/96gl03021>
- Mao, Z., Lin, J.-F., Liu, J., & Prakapenka, V. B. (2011). Thermal equation of state of lower-mantle ferropericlase across the spin crossover. *Geophysical research letters*, 38(23), n/a. <https://doi.org/10.1029/2011gl049915>
- Marquardt, H., Speziale, S., Reichmann, H. J., Frost, D. J., & Schilling, F. R. (2009). Single-crystal elasticity of (Mg0.9Fe0.1)O to 81 GPa. *Earth and planetary science letters*, 287(3-4), 345–352. <https://doi.org/10.1016/j.epsl.2009.08.017>
- Mashino, I., Murakami, M., Miyajima, N., & Petitgirard, S. (2020). Experimental evidence for silica-enriched Earth's lower mantle with ferrous iron dominant bridgmanite. *Proceedings of the National Academy of Sciences of the United States of America*, 117(45), 27899–27905. <https://doi.org/10.1073/pnas.1917096117>
- McNamara, A. K., Garnero, E. J., & Rost, S. (2010). Tracking deep mantle reservoirs with ultra-low velocity zones. *Earth and planetary science letters*, 299(1-2), 1–9. <https://doi.org/10.1016/j.epsl.2010.07.042>
- Mosegaard, K., & Tarantola, A. (1995). Monte Carlo sampling of solutions to inverse problems. *Journal of geophysical research*, 100(B7), 12431–12447. <https://doi.org/10.1029/94jb03097>

- Murakami, M., Hirose, K., Kawamura, K., Sata, N., & Ohishi, Y. (2004). Post-Perovskite phase transition in MGSIO₃. *Science*, 304(5672), 855–858. <https://doi.org/10.1126/science.1095932>
- Murakami, M., Ohishi, Y., Hirao, N., & Hirose, K. (2012). A perovskitic lower mantle inferred from high-pressure, high-temperature sound velocity data. *Nature*, 485(7396), 90–94. <https://doi.org/10.1038/nature11004>
- Nakagawa, T., & Tackley, P. J. (2011). Effects of low-viscosity post-perovskite on thermo-chemical mantle convection in a 3-D spherical shell. *Geophysical research letters*, 38(4), n/a. <https://doi.org/10.1029/2010gl046494>
- Nomura, R., Hirose, K., Uesugi, K., Ohishi, Y., Tsuchiyama, A., Miyake, A., & Ueno, Y. (2014). Low Core-Mantle Boundary Temperature Inferred from the Solidus of Pyrolite. *Science*, 343(6170), 522–525. <https://doi.org/10.1126/science.1248186>
- Sambridge, M., & Mosegaard, K. (2002). MONTE CARLO METHODS IN GEOPHYSICAL INVERSE PROBLEMS. *Reviews of geophysics*, 40(1). <https://doi.org/10.1029/2000rg000089>
- Shephard, G. E., Houser, C., Hernlund, J. W., Valanis-Cardon, J. J., Trønnes, R. G., & Wentzcovitch, R. M. (2021). Seismological expression of the iron spin crossover in ferropericlase in the Earth's lower mantle. *Nature communications*, 12(1). <https://doi.org/10.1038/s41467-021-26115-z>
- Sturhahn, W., Jackson, J. M., & Lin, J. F. (2005). The spin state of iron in minerals of Earth's lower mantle. *Geophysical research letters*, 32(12). <https://doi.org/10.1029/2005gl022802>
- Su, W.-J., & Dziewonski, A. M. (1997). Simultaneous inversion for 3-D variations in shear and bulk velocity in the mantle. *Physics of the earth and planetary interiors*, 100(1-4), 135–156. [https://doi.org/10.1016/s0031-9201\(96\)03236-0](https://doi.org/10.1016/s0031-9201(96)03236-0)
- Trampert, J., Deschamps, F., Resovsky, J., & Yuen, D. (2004). Probabilistic tomography maps chemical heterogeneities throughout the lower mantle. *Science*, 306(5697), 853–856. <https://doi.org/10.1126/science.1101996>
- Trampert, J., & Fichtner, A. (2013). Global Imaging of the Earth's Deep Interior: Seismic Constraints on (An)isotropy, Density and Attenuation. *Physics and Chemistry of the Deep Earth*, 324–350. <https://doi.org/10.1002/9781118529492.ch11>
- Trautner, V. E., Stackhouse, S., Turner, A. R., Koelemeijer, P., Davies, D. R., Méndez, A. S. J., Satta, N., Kurnosov, A., Liermann, H.-P., & Marquardt, H. (2023). Compressibility of ferropericlase at high-temperature: Evidence for the iron spin crossover in seismic tomography. *Earth and planetary science letters*, 618, 118296. <https://doi.org/10.1016/j.epsl.2023.118296>
- Tromp, J. (2019). Seismic wavefield imaging of Earth's interior across scales. *Nature reviews. Earth environment*, 1(1), 40–53. <https://doi.org/10.1038/s43017-019-0003-8>
- Tsuchiya, T., Wentzcovitch, R. M., Da Silva, C. R. S., & De Gironcoli, S. (2006). Spin transition in magnesiowüstite in Earth's lower mantle. *Physical review letters*, 96(19). <https://doi.org/10.1103/physrevlett.96.198501>
- Wentzcovitch, R. M., Justo, J. F., Wu, Z., Da Silva, C. R. S., Yuen, D. A., & Kohlstedt, D. (2009). Anomalous compressibility of ferropericlase throughout the iron spin cross-over. *Proceedings of the National Academy of Sciences of the United States of America*, 106(21), 8447–8452. <https://doi.org/10.1073/pnas.0812150106>
- Wu, Z., Justo, J. F., Da Silva, C. R. S., De Gironcoli, S., & Wentzcovitch, R. M. (2009). Anomalous thermodynamic properties in ferropericlase throughout its spin crossover. *Physical review. B, Condensed matter and materials physics*, 80(1). <https://doi.org/10.1103/physrevb.80.014409>

- Wu, Z., & Wentzcovitch, R. M. (2014). Spin crossover in ferropericlase and velocity heterogeneities in the lower mantle. *Proceedings of the National Academy of Sciences of the United States of America*, 111(29), 10468–10472. <https://doi.org/10.1073/pnas.1322427111>

Under Review